Subcortical circuit dysfunctions delay perceptual decision-making in autism models

Laura E. Burnett[1], Peter Koppensteiner[1], Olga Symonova[1], Tomás Masson[1], Tomas Vega-Zuniga[1], Ximena Contreras[1], Thomas Rülicke[2], Ryuichi Shigemoto[1], Gaia Novarino[1], Maximilian Jösch[1#].

[1] Institute of Science and Technology Austria; Am Campus 1, 3400 Klosterneuburg, Austria.

[2] Institute of Laboratory Animal Science, University of Veterinary Medicine Vienna; Veterinärplatz 1, 1210 Vienna, Austria.

[#]Correspondance: maxjosch@ist.ac.at

Autism spectrum disorders (ASD) include a range of neurodevelopmental conditions characterised by social and communication difficulties[1], often co-occurring with sensory processing abnormalities[2]. The neural origins of these impairments are thought to reside in cortical circuits[3–5]. Here we demonstrate that a subcortical node required to initiate efficient and timely responses to visual threats is disrupted across genetic models of ASD. Although mutant mice can detect visual threat stimuli, they require longer to evaluate them and respond with less vigour than their wild-type siblings. These delays in perceptual judgement are linked to reduced place-aversion to visual threats. Visual responses and other motor properties remain unaffected, overall indicating cognitive rather than sensory or motor impairments. Focusing on one of the models (*Setd5*), we show that these behavioural deficits are recapitulated following optogenetic activation of excitatory deep medial collicular neurons, known to initiate threat responses by exciting the dorsal periaqueductal grey (dPAG). Consistently, *ex vivo* patch-clamp recordings of *Setd5* mutant dPAG neurons revealed a stark hypoexcitability phenotype mediated by misregulation of a voltage-gated potassium channel. Similar physiological characterisation across ASD models demonstrates that different molecular mechanisms converge on similar behavioural phenotypes. Our results show that the timing of perceptual decision-making is regulated via intrinsic excitability and emphasise the use of an innate behaviour to mechanistically dissect cognitive disorders.

Autism spectrum disorders (ASD) are conditions characterised by challenges with social interactions and repetitive behaviours, reflected in inadequate responses to others' mental states and emotions[1]. These alterations in social cognition co-occur with disordered sensory processing[2], a widespread yet often overlooked feature across ASD observed in every sensory modality[6]. In the visual domain, affected individuals frequently exhibit difficulties with visual attention and hyper- or hyposensitivity to visual stimuli[7], and mounting evidence suggests that the circuits involved in visual information processing are disrupted[8]. For example, atypical neuronal responses to faces and looming stimuli have been observed in individuals with ASD[9–11]. Such sensory deficits directly affect visually-guided behaviours such as gaze control, which emerges at a few months of age[12] and forms a prominent diagnostic feature[13]. Changes in gaze dynamics to subliminal stimuli[14] indicate that neuronal circuits mediating subconscious visual responses are affected, pointing towards subcortical circuits, particularly the superior colliculus (SC)[8,15,16].

Deficits in sensation are seemingly separate phenomena from the more studied cognitive impairments in ASD, believed to arise from cortical malfunctions[3–5]. However, their close association is indicative of the possibility of a common underlying thread. Such evidence has recently implicated SC-pathway impairments with atypical sensory and cognitive processing[8,16]. Given this evidence, we decided to directly explore the relationship between sensation and cognition in ASD within an innate, robust and reproducible sensorimotor transformation known to be mediated by the SC - the looming avoidance response (LAR)[17,18]. Our results show that molecularly distinct ASD mouse models (*Setd5*[19], *Cul3*[20] and *Ptchd1*[21]) present similar deficits in LAR that are not due to direct sensory or motor deficits. While all animals immediately detect the looming stimulus and can respond vigorously to a threat, they require longer to initiate the escape response than their wild-type siblings. In *Setd5*$^{+/-}$, these deficits emerge due to changes in the intrinsic properties of neurons in the dorsal periaqueductal grey

(dPAG), a structure known for commanding escape responses and to receive direct input from the SC[22,23]. These changes affect the proper generation of perceptual decisions, linking a sensorimotor disorder via a defined molecular mechanism to cognitive dysfunction and associating the dPAG with ASD.

Delayed looming avoidance responses across ASD models.

To investigate whether subcortical visual circuits could be affected in mouse models of ASD, we evaluated the behavioural responses to the innate looming avoidance response (LAR) paradigm. LAR is largely independent of cortical input, requiring the SC and its downstream targets to initiate appropriate responses. For this purpose, we tested three genetic ASD mouse models affecting independent biological pathways. Whereas *SET-domain containing 5 (Setd5)*[19] is a histone-associated protein, *Cullin3* (*Cul3*)[20] is a ubiquitin ligase-encoding gene and *Ptchd1*[21] is a member of the Patched family and speculated to function as a Sonic hedgehog receptor. Disruption of any one has been found in ~1 % of patients with intellectual disability and ASD[19–21]. We subjected mutants (i.e., *Setd5*$^{+/-}$, *Cul3*$^{+/-}$, *Ptchd1*$^{Y/-}$) and their wild-type (WT) siblings to our LAR paradigm, where mice would automatically trigger a sequence of five consecutive looms upon entering a threat zone (Fig. 1a, see methods). For all experiments, we only used animals without any eye abnormalities, which are described to sometimes occur in *Setd5* mutant animals[19]. During the acclimatisation period, all animals showed similar exploratory behaviour and dynamics, with the exception of *Ptchd1*, which showed a baseline hyperactivity phenotype[21] (Supplementary Fig. 5). At first glance, all cohorts had seemingly similar behavioural responses, escaping to the shelter upon stimulus presentation (Suppl. Video 1). However, behavioural differences between the genotypes became evident when observing their reaction times (Fig. 1b, Supplementary Figs. 1d,2a & 3d). While WT siblings responded robustly to the first stimulus presentation, their heterozygous siblings required, on average, more repetitions to elicit an escape response, had longer reaction times between the stimulus start and the maximum speed, and displayed slower vigour, as represented by their maximal speed[24] (Fig. 1c,d,g, Supplementary Figs. 1e,f, j & 2b,c,g). Slower reaction times and reduced vigour could also be observed in *Ptchd*$^{Y/-}$ animals, despite their baseline hyperactivity. This difference in response reaction time is an intrinsic and not an adaptive property since it is present during the first loom presentation (Fig. 1h, Supplementary Figs. 1g & 2d), and varied in strength, with *Cul3*$^{+/-}$ mice showing a less severe phenotype than the *Setd5* or *Ptchd1* models. The differences across genotypes were robust across trials and days (Fig. 2d-e, Supplementary Figs. 1h & 2e) and independent of the location, head direction, or speed of the animal at stimulus onset (Supplementary Fig. 4). Excluding *Ptchd1*, an X-linked gene for which we analysed only males, these differences are sex-independent (Fig. 1a - females, and Supplementary Fig. 3d-i - males). The overall escape kinetics were indistinguishable among all genotypes (Fig. 1f, Supplementary Figs. 1i & 2f), despite having different reaction times and maximal speeds (Fig. 1g,h, Supplementary Figs. 1f,g & 2c,d). Only *Cul3*$^{+/-}$ mice had a slightly slower acceleration (Supplementary Fig. 2d, f), in line with their previously described stride defects[20]. This indicates that the escape delay differences are deficits in perceptual decision-making and not due to intrinsic motor deficits, showing that the LAR can serve as a robust behavioural assay to uncover the underlying circuit dysfunctions across ASD models.

To test whether the delay in initiating an escape to the loom was due to the mutant mice simply detecting the stimulus later than their WT siblings, we examined the immediate change in the speed of the animals from the time of the first loom, selecting only the trials where the mice performed an escape to the shelter at any point during the looming events. As expected, WT animals showed an increase in speed immediately following the stimulus onset. In contrast, across all mutant animals we saw an arrest behaviour immediately following the appearance of the stimulus (Fig. 1i-k, right panels). This arrest behaviour is not the known freezing behaviour, another commonly observed response to the looming stimulus characterised by the complete lack of any movement over an extended time period. Instead, during the arrest, animals can still make small and slow movements of the head and upper body (see Supplementary Videos), a behaviour that is indicative of an ongoing

evaluation of the threat level as previously shown for loom stimuli of different contrast[24]. This suggests that the delay in LAR arises from difficulties in evaluating the threat level or the stimulus. The vigour of escape, on the other hand, was only minimally reduced between cohorts, showing a clear separation to the immediate response of the first loom into either an escape or an arrest response for WT and ASD animals, respectively (Fig. 1i-k, left panels). Thus, these results show that all genotypes detected a stimulus change within a similar timeframe to their WT littermates.

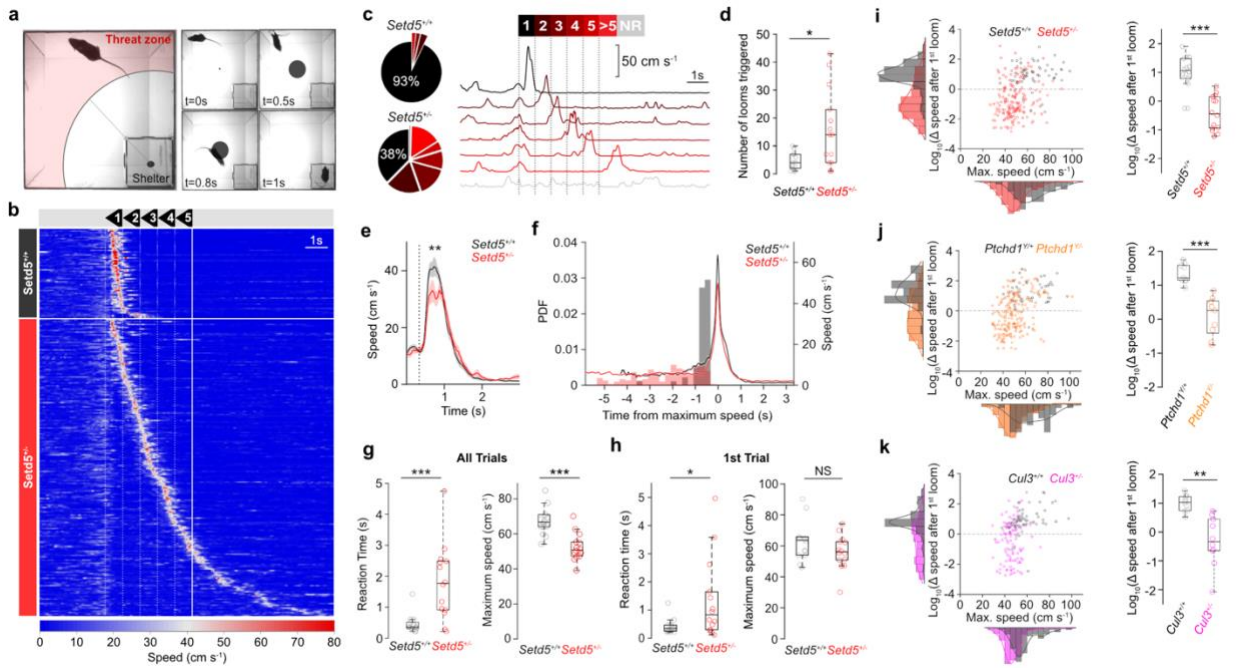

Figure 1. ASD mice exhibit delayed and less vigorous looming avoidance responses. a, Video frames from a single trial of the looming avoidance response (LAR) paradigm showing the location of the shelter and the threat zone (left). Frames from a trial, covering one second after the triggering of the looming stimulus, t = 0 s (right). **b**, Raster plot of mouse speed in response to the looming stimuli (white, dotted vertical lines denote the start of each loom; solid white line denotes the end of the stimulus) for *Setd5*$^{+/+}$ (top, 60 trials) and *Setd5*$^{+/-}$ (bottom, 198 trials), sorted by reaction time. **c**, Proportion of trials where the mice respond within 1 of the 5-loom stimuli, after the 5th, or not at all (left, $p < 0.001$). Example velocity profiles from each category (right). **d**, Summary of mean total looms triggered per genotype across 5 days of testing (*Setd5*$^{+/+}$: 4.36 looms; *Setd5*$^{+/-}$: 16 looms, P = 0.013). **e**, Mean response speed of *Setd5*$^{+/+}$ (55 trials) and *Setd5*$^{+/-}$ (38 trials) for trials where the mice respond within the first loom presentation (maximal speed difference: P = 0.009). **f**, Mean speed response profiles of all trials where mice escape to the shelter, showing similar escape kinetics, with a histogram of the distribution of the start of the loom stimulus aligned to the peak of the escape response (*Setd5*$^{+/+}$, 61 trials; *Setd5*$^{+/-}$, 198 trials, $p < 0.001$). **g**, Mean reaction time (left) and maximum escape speed (right) per animal, for all trials where the mouse responded (reaction time, P = 0.001; maximum escape speed, $P < 0.001$). **h**, Mean reaction time (left) and maximum escape speed (right) per animal, for the first ever loom presentation (reaction time ,P = 0.046; maximum escape speed, P = 0.166) **i**, Scatter-hist plot of the $\log_{10}$(change in speed upon the 1st loom presentation) (x-axis, see methods) and the maximum speed reached during the escape (y-axis), (left: Log_{10}(**Δ**Speed), $p < 0.001$; maximum escape speed, $p < 0.001$, right: Log_{10}(**Δ**Speed), $p < 0.001$). Right, summary of the average $\log_{10}$(**Δ**Speed) per animal ($P < 0.001$). **j-k**, as for (**i**) but for the *Ptchd1* and *Cul3* mouse models, respectively (**j**, left: Log_{10}(**Δ**Speed), $p < 0.001$; maximum escape speed, $p < 0.001$, right: Log_{10}(**Δ**Speed), $p < 0.001$; **k**, left: Log_{10}(**Δ**Speed), $p < 0.001$; maximum escape speed, $p < 0.001$, right: P = 0.002). Box-and-whisker plots show median, IQR and range. Shaded areas show s.e.m.. P-values: Wilcoxon's test, p-values: two-sample KS test. For detailed statistics, see supplementary table 1.

Given that cortical malfunctions have been suggested as the cause of sensory differences in autism[3-5] and that the visual cortex has been shown to modulate the response magnitude of looming sensitive cells in the SC[25], we tested whether the behavioural responses are affected in cortex and hippocampus-specific conditional *Setd5* animals (*Setd5*$^{+/fl}$; *Emx1*-Cre, Supplementary Fig. 6a-b). These animals showed no behavioural differences in their reaction times, vigour, or response kinetics (Supplementary Fig. 6c-e), indicating that subcortical pathways, namely the SC and PAG, and not cortical areas are in dysfunction.

Repetitive looming avoidance responses across ASD models.

Although the innate LAR does not require learning, repeated loom presentations cause adaptive behavioural changes, for example, the emergence of aversive place avoidance of the threat zone[24]. Given that ASD animals triggered three times more looming events than their WT siblings (Fig. 1d, Supplementary Figs. 1j, 2g & 3d), we explored if altered adaptation to repeated presentations could account for the observed difference in average reaction time and vigour (Fig. 1g, Supplementary Figs. 1g & 2d). For that purpose, we compared the intrinsic behavioural characteristics and the effect of the LAR on the exploration strategies and behavioural adaptations across days (Fig. 2a, Supplementary Figs. 1k & 2h). Before stimulus exposure, all genotypes traversed the arena, left the shelter, and remained outside of the shelter for similar extents of time (Supplementary Figs. 1l, 2i, 3a-c (day 0) & 5), indicating that their innate exploration strategies cannot account for the differences in reaction time and vigour. WT animals showed expected reductions in their exploratory behaviour following the initial exposure to the looming stimulus, staying closer, making fewer exits, and staying outside of the shelter for a shorter period than during the pre-stimulus exploration time (Supplementary Figs. 1l, 2i & 3a-c), eliciting fewer looms in total (Fig. 2c) with relatively constant reaction time and response vigour (Fig. 2d-e). Strikingly, ASD animals consistently triggered more looms and had no signs of sensitisation upon repeated exposures (Fig. 2c-e, Supplementary Figs. 1h, 2e). After the initial decrease in exploration following the first stimulus presentation, they showed no further consolidation of the place aversion to the threat zone (Supplementary Figs. 1l, 2i & 3a-c). The reaction time and vigour of the escape response remained longer and slower across days (Fig. 2d-e), respectively, indicating that ASD animals do not sensitise as their WT siblings do to the LAR paradigm. Importantly, the reaction time, but not the escape vigour, was different at the very first presentation of the looming stimulus (Fig. 1h, Supplementary Fig. 1g), showing that the differences in LAR are mediated by intrinsic factors, whereas differences in response vigour arise due to adaptation of the response. *Cul3*$^{+/-}$ also show a similar trend, but their response dynamics are slightly different, possibly related to the previously described motor impairments (Supplementary Fig. 1g, j).

We next tested if the delayed perceptual decisions (Fig.1) are related to the consolidation of place aversion (Fig. 2a, Supplementary Fig. 3a-c), two seemingly independent behaviours. We analysed the average number of shelter exits for each animal and compared them with their average reaction times and vigour (Fig. 2f, g). Surprisingly, the strength of the place aversion was a strong predictor of the reaction times, but not vigour, indicating that the timing of the perceptual decision is instructive for appropriate conditioning.

To assess the limits of response adaptation and to ascertain if the presence of a reward would overcome the place aversion, we conducted the same behavioural experiment but with the presence of a food reward on the far side of the arena within the threat zone (Fig. 2h), and with no inter-stimulus interval restriction. Although WT siblings did make some attempts to retrieve the food reward, they quickly sensitised, rarely leaving the shelter and were unsuccessful in obtaining the food reward. ASD animals, on the other hand, increased their shelter leaving events, in many cases persisting until reaching the reward (Fig. 2i-k, Suppl. Video 2). Despite the rapid and repeated exposure, Setd5$^{+/-}$ mice continued to escape to the shelter upon stimulus presentation, for >20 consecutive presentations, with their reaction times mildly adapting (Fig. 2l top) and vigour remaining largely constant (Fig. 2l bottom), indicating that differences in response vigour do not arise over repeated consecutive

exposures. Recent work has shown that repeated and consecutive presentations of the looming stimulus with increasing saliency can lead to a learned suppression of escape behaviour (LSE)[26]. Given that Setd5$^{+/-}$ animals do not adapt to repeated and consecutive presentations of high contrast looming in the presence of a reward (Fig. 2i-l), we tested if LSE-protocol would elicit any adaptation to the LAR in the absence of a reward. We exposed both genotypes to a milder version of this LSE paradigm and then tested their responses to the standard high contrast stimuli (Fig. 2m). We found that after exposure to our LSE paradigm, *Setd5*$^{+/+}$ mice were indistinguishable in their reaction times and escape vigour from Setd5$^{+/-}$ mice before the paradigm. Similarly, we observed that *Setd5*$^{+/-}$ mice can adapt, reducing their reaction time and vigour after. The main difference was a robust change in the starting baseline (Fig. 2m-p), indicating that a mechanism contributing to LSE is already active in Setd5$^{+/-}$ mice.

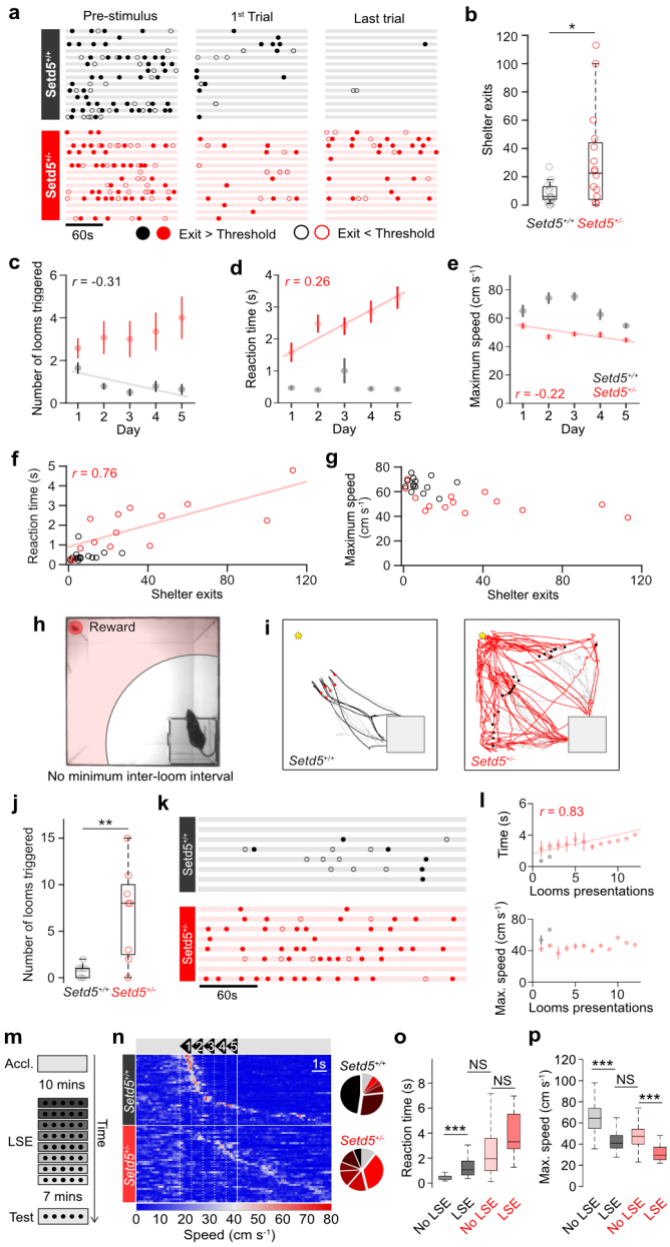

Figure 2. Altered adaptation and repetitive behavioural phenotype to the LAR. a, Exploratory behaviour during acclimatisation, first and last trial of the LAR paradigm. Each row represents one animal, filled and open dots represent exits into the threat zone or not, respectively. **b**, Summary of mean total shelter exits across the 5 test days (*Setd5*$^{+/+}$, 6.0; *Setd5*$^{+/-}$, 24.5, P = 0.019). **c-e**, Adaptation in the average number of looms triggered, escape dynamics and maximum speed across days (**c**, *Setd5*$^{+/+}$, p = 0.0087; Setd5$^{+/-}$, p = 0.2192; **d**, *Setd5*$^{+/+}$, p = 0.890; Setd5$^{+/-}$, p < 0.001; **e**, *Setd5*$^{+/+}$, p = 0.121; *Setd5*$^{+/-}$, p = 0.002). **f**, Relationship between the number of shelter exits and the average reaction time per animal (*Setd5*$^{+/+}$, p = 0.626; *Setd5*$^{+/-}$, p = 0.002). **g**, Relationship between the number of shelter exits and the maximum escape speed per animal (*Setd5*$^{+/+}$, p = 0.547; *Setd5*$^{+/-}$, p = 0.053). **h**, Video frame from a reward trial showing the location of the food reward within the threat zone. **i**, Example trajectories during the reward trials showing the position of the mouse for the 3 s before triggering the loom (light grey) and for the 6 s following the stimulus start (black or red). Filled dots represent the position of the mouse when the stimulus was triggered, grey square is the shelter, the yellow star shows the position of the food reward. **j**, Number of looms triggered during the reward trial (*Setd5*$^{+/+}$, 1 bout; *Setd5*$^{+/-}$, 8 bouts, P = 0.005). **k**, Ethograms of exits during the reward trials show an increased probability of leaving the shelter during the trial (number of exits, 2.12

for *Setd5*$^{+/+}$, 6.88 for *Setd5*$^{+/-}$, p = 0.057). **l**, Reaction time (top panel, *Setd5*$^{+/-}$, 44 trials, $r = 0.828$, $p = 0.0001$) and escape vigour (bottom panel, *Setd5*$^{+/-}$, 44 trials, $r = 0.184$, $p = 0.5116$) during repeated presentations of the loom. Trials when the animal was interacting with the reward were excluded. **m**, Learned suppression of escape (LSE) paradigm. **n**, Left, raster plot of mouse speed to the loom stimulus, as in Fig. 1b but after LSE. Right, proportion of trials where the mice respond within 1 of the 5-loom stimuli, after the 5th, or not at all. **o**, LSE results in slower reaction times in *Setd5*$^{+/+}$ ($P < 0.001$, Kruskal-Wallis (K-W) test), comparable to that of *Setd5*$^{+/-}$ before LSE ($P = 0.319$, K-W test). LSE does not cause a significant change in the reaction time of *Setd5*$^{+/-}$ mice (P = 0.082, K-W test). **p**, LSE results in slower maximum speeds in both genotypes (*Setd5*$^{+/+}$, $P < 0.001$; *Setd5*$^{+/-}$, P < 0.001, K-W test). Max. speed after LSE in *Setd5*$^{+/+}$ is comparable to that of *Setd5*$^{+/-}$ before LSE ($P = 0.386$, K-W test). Box-and-whisker plots show median, IQR and range. P-values: Wilcoxon's test, p-values: Pearson's test, unless specified. Plotted linear fits depict the statistically significant correlations. For detailed statistics, see Supplementary Table 1.

Intact visual response properties across ASD models.

Changes in average reaction times have previously been shown to depend on the saliency of the threat stimulus. Whereas repeated high-contrast looming stimuli evoke strong LAR, low-contrast looms drive less vigorous escapes and longer reaction times[24], suggesting that deficits in visual processing could underlie the behavioural disorders observed in ASD mice. This possibility is aggravated by the fact that the expression of genes involved in eye development are known to be misregulated in *Setd5*$^{+/-}$ animals[19]. To explore possible visual response changes, we recorded visually-evoked responses across different layers of the SC, using 32-channel silicon probes in head-fixed, awake-behaving animals (Fig. 3a-c), and determined the recording depth using current source density analysis (Fig. 3b). In our setup, mutant and control animals had similar running probabilities and showed similar baseline firing properties (Fig. 3d). We next assessed visual response properties to full-field flashes, visual stimuli that drive all neurons similarly irrespective of their receptive field positions. First, we show that pupil dynamics are unaffected across genotypes (Fig. 3e). Next, when clustering visually responsive cells into 10 clearly defined groups, we could observe similar relative proportions and identical response properties (Fig. 3f-g, Supplementary Fig. 8a-c, 8k-m). Identical responses were also observed in their spatio-temporal receptive fields as well as the proportion of ON and OFF responsive cells (Supplementary Fig. 7c-g). Direction-selective responses, either to bars or gratings (Supplementary Figs. 7i-n), were also indistinguishable across groups. Finally, we explored the response properties to looming stimuli across SC layers. Looms elicit robust and reproducible firing across genotypes (Fig. 3h), with similar firing, peak rates and time-to-peak responses across genotypes (Fig. 3i-k, Supplementary Fig. 8g-i & 8q-s). The overall response kinetics (Fig. 3i, Supplementary Fig. 8e,o) as well as the adaptation in average firing rates across presentations (Fig. 3m,n, Supplementary Fig. 8f,j,p,t) were indistinguishable across genotypes. The lack of any reportable visual response difference across the SC layers indicates that retino-colliculuar visual processing is largely unaltered and excludes the possibility that sensory processing can account for the observed visuomotor deficits.

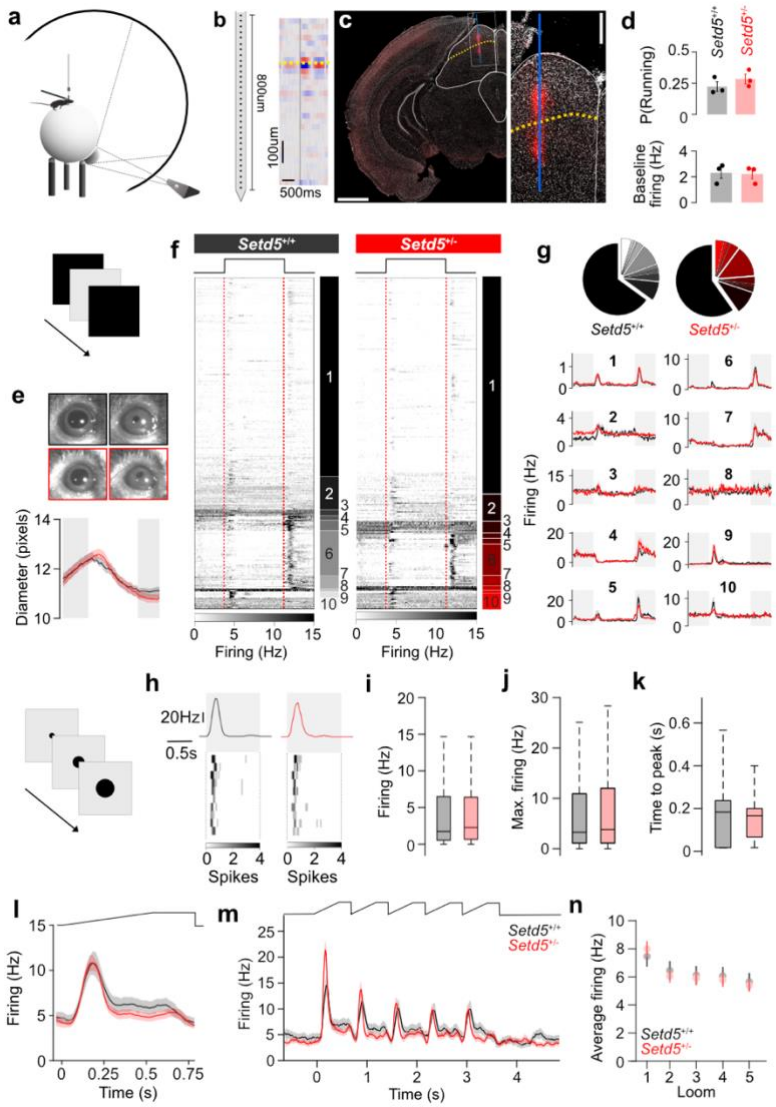

Fig. 3. Intact visual processing across the SC. a, Schematic of the *in vivo* recording setup displaying the spherical treadmill and light projector illuminating the spherical screen. **b**, Left, Schematic of the 32-channel silicon probe used to record extracellular activity aligned with the current source density analysis of a single flash stimulus averaged over 10 presentations. Black vertical line represents the stimulus onset, yellow dotted line marks the inflection depth separating the current source and sink. **c**, Histological reconstruction of the probe position marked with DiI (120 µm coronal section, scale bar: 1000 µm) with a close-up (scale bar: 250 µm). Yellow dotted line as in (**b**). **d**, Proportion of time the mice were moving during the recording sessions (P = 0.400, top) and SC's baseline firing rate (P = 0.880, bottom). **e**, Pupil dilation in response to the full-field flash stimulus. Example images of dilated and constricted pupils in responses to the OFF (left) and ON (right) periods of the flash. Setd5$^{+/+}$ (black), Setd5$^{+/-}$ (red) (P = 0.060). **f**, Sorted raster plot of neural responses to a single flash stimulus. Vertical red dotted lines indicate the on and offset of the flash stimulus. **g**, Proportion of cells in each cluster (top). Mean ± s.e.m. of the flash responses in each cluster (traces). **h**, Example responses. Mean and spike raster plots of units in Setd5$^{+/+}$ (black) and Setd5$^{+/-}$ (red) to a single loom stimulus. **i-k**, Summary of mean, maximum and time-to-peak firing (**i**, P = 0.215; **j**, P = 0.100; **k**, P = 0.372). **l**, Mean±s.e.m. response of all and (**m**) of the 5 consecutive loom stimuli for Setd5$^{+/+}$ (black) and Setd5$^{+/-}$ (red) units. **n**, Average firing to a single loom across the 5-loom stimulus (p = 0.732) P-values: Wilcoxon's test, p-values: two-way repeated measures ANOVA. For detailed statistics, see Supplementary Table 1.

Optogenetic stimulation of deep medial SC replicates response delay in Setd5.

The lack of sensory response differences in the SC suggests that the main cause of the behavioural difference may reside in downstream areas. Given that the dorsal periaqueductal grey (dPAG) encodes for the choice of escape and controls the escape vigour[24], we hypothesised that optogenetic stimulation of the dPAG projecting SC cells should recapitulate some of the described behavioural differences observed in the ASD models. To test this, we focused on the *Setd5* mouse line and used unilateral *in vivo* channelrhodopsin-2 (ChR2) activation of $VGluT2^{+}$ cells in the deep medial SC (dmSC) (Fig. 4a, Supplementary Fig. 9a-c). In line with previous findings, activation of dmSC neurons in $Setd5^{+/+}$ animals instructed immediate shelter-directed escapes (Fig. 4b, left & 4c) and were absent in controls (Supplementary Fig. 9d-h) Gradually increasing the laser power and thus, optogenetic activation, led to corresponding increases in the escape probability (Fig. 4d), the escape vigour (Fig. 4e) and decreases in the latency to respond (Fig. 4f). By contrast, activation of dmSC neurons in the $Setd5^{+/-}$ background, more often resulted in an initial arrest, followed by shelter seeking escape responses (Fig. 4b, right & 4c, g), mimicking the behavioural divergence observed for LAR (Fig. 1). Interestingly, this behavioural difference was evident only during strong optogenetic activations. At lower laser intensities, both genotypes exhibited a transition from arrest to weak escape behaviours (Fig. 4c, g) with similarly low vigour (Fig. 4e) and reaction time (Fig. 4f). Given that changes in the strength of optogenetic activation mimic LAR to looms of different contrast[24], we hypothesised that when probing animals to LAR of different contrasts, both genotypes should show similar responses at lower contrast (Fig. 4h). For this purpose, we tested the LAR to three different contrast levels: 98 %, 50 % and 20 % (Fig. 4i). As predicted, the LAR to low-contrast looms did not differ across genotypes, showing similar response speeds and reaction times (Fig. 4i). Remarkably, in $Setd5^{+/-}$ animals, these parameters remained constant across contrast levels, suggesting that action initiation mechanisms, and not visual transformations, are disrupted. Overall, these results emphasise that the differences observed in this behaviour are mediated by altered processing in the dPAG.

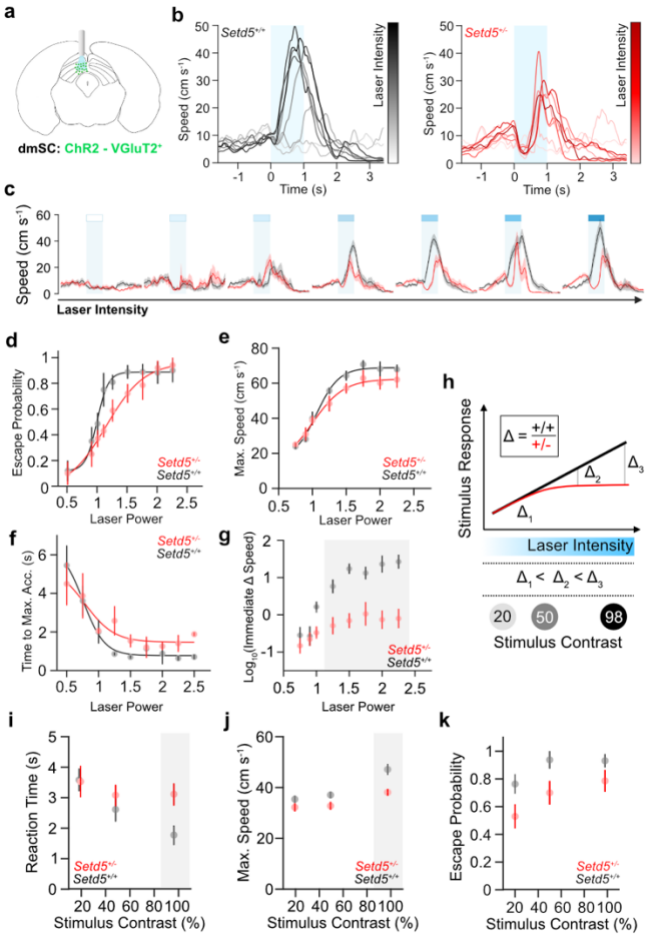

Figure 4. Optogenetic activation of deep SC neurons recapitulates LAR differences. **a**, Schematic of ChR2 expression in the dmSC and implantation of the optic fibre. **b**, Mean speed responses to optogenetic stimulation at increasing laser intensities. Blue shaded areas show the laser stimulation times. **c**, Subplots of trials in (**b**) (l-r, low to high intensity). **d-g**, Psychometric, vigour and chronometric curves (**d,** Setd5$^{+/+}$, 312 trials, n = 4, slope=4.62, 95% confidence interval (2.87, 6.37); Setd5$^{+/-}$, 291 trials, n = 4, slope = 1.36, 95 % confidence interval (0.62, 2.11); **e**, Setd5$^{+/+}$, 195 trials, n = 4, slope = 2.63, 95 % confidence interval (0.90, 4.36); Setd5$^{+/-}$, 171 trials, n = 4, slope = 1.88, 95 % confidence interval (0.44, 3.31); **f**, Setd5$^{+/+}$: 195 trials, n=4, slope = 2.58, 95 % confidence interval (0.94, 4.22); Setd5$^{+/-}$, 171 trials, n = 4, slope = 1.88, 95 % confidence interval (-1.99, 5.76). **g**, Mean ± s.e.m. of the change in speed (300-800 ms after laser onset) at different intensities (between genotype distributions: $p < 0.001$; grey area denotes statistically significant difference through multiple comparisons test). **h**, Schematic of the divergence between genotypes with increasing stimulus intensity (laser or loom). **i-k**, Summary of mean ± s.e.m. of (**i**) vigour, (**j**) reaction time and (**k**) escape probability responses to LAR at different stimulus intensities. (**i**, between genotypes: $p < 0.001$, between contrast: $p = 0.003$, **j,** between genotypes: $p = 0.021$, between contrast: $p = 0.015$; **k**, between genotypes: $p < 0.001$, between contrast: $p = 0.005$; grey area denotes statistically significant difference through multiple comparisons test). Lines are sigmoidal fits pooled across trials from all mice and binned according to light intensities. Error bars and shaded areas represent s.e.m. p-values: Two-way repeated measures ANOVA with multiple comparisons with Bonferroni correction. For detailed statistics, see Supplementary Table 1.

Hypoexcitability in dPAG neurons is due to Kv misregulation

Our previous results point toward the direct involvement of the dPAG in the delayed LAR response. To test if any synaptic or intrinsic properties of dPAG neurons are impaired, we performed whole-cell patch-clamp recordings in slices (Fig. 5a). First, using the same animals used for optogenetic stimulation *in vivo*, we tested if the synaptic properties of dmSC inputs to the dPAG are changed. 10 Hz *ex vivo* optogenetic activation elicited monosynaptic excitatory postsynaptic current (EPSC) with an average current of −244±9.65 pA in *Setd5*$^{+/+}$ and -228±11.8 pA in *Setd5*$^{+/-}$ (Fig. 5a,b), larger than previously reported[24]. At this frequency, repeated stimulations showed no facilitation in both genotypes (Fig. 5b), indicating that dmSC inputs to the dPAG are unaltered. Next, we explored spontaneous neurotransmission by recording sEPSCs. Again, the sEPSC frequency, amplitude, rise, and decay time were unaltered (Supplementary Fig. 10b-e), supporting the view that the synaptic properties remain similar at a circuit level. Finally, we probed the intrinsic properties of dPAG neurons. Although the membrane potential, input resistance, membrane constant, and capacitance were identical between genotypes (Fig. 5c), we observed a stark decrease in the ability of these cells to generate action potentials in response to injected current (Fig. 5d), without affecting the rheobase (Supplementary Fig. 10f). These changes were accompanied by changes in the spike shape of Setd5$^{+/-}$ animals (Fig. 5e,f) that showed slightly higher depolarisation, lower after-hyperpolarisation and slower rise dynamics in comparison to their WT siblings (Fig. 5g). Based on prior work we know that stronger dPAG activation leads to more vigorous escapes and that the underlying biophysical mechanisms depend on dPAG neuronal synaptic integration and excitability[24]. Thus, changes in excitability are a proxy of the expected escape strength. Remarkably, the response characteristics of dPAG neurons in *Setd5*$^{+/+}$ *and Setd5*$^{+/-}$ match their behavioural differences (Figs. 1 & 4). At weak current-injections (Fig. 5d), optogenetic activation (Fig. 4b-g) or low contrast looms (Fig. 4i), both genotypes are indistinguishable from each other. However, at stronger current-injections, optogenetic activation or high contrast looms, *Setd5*$^{+/+}$ *and Setd5*$^{+/-}$ diverge, with an hypoexcitability phenotype for *Setd5*$^{+/-}$ (Fig. 5d) that matches the delay in LAR for optogenetic (Fig. 4g) and visual (Figs. 1, 4i) activation.

To determine if the hypoexcitability phenotype was a brain-wide phenomenon, we patched dmSC interneurons (Supplementary Fig. 10g-l). Here, we observed a weaker and statistically non-significant hypoexcitability trend, indicating that the strength of the effect is area specific. Next, we investigated the underlying mechanisms of the hypoexcitable phenotype of the *Setd5*$^{+/-}$ PAG cells. The changes in excitability and spike kinetics are indicative of differences in channel composition that are part of adaptive homeostatic mechanisms[27], suggesting the influence of voltage-gated potassium channels (Kv). Previously published work[19], which studied the transcriptomic changes brought about by a mutation in *Setd5*$^{+/-}$, highlighted significant upregulation in the expression of Kv1.1. To test whether the blockade of Kv1.1 channels would be able to rescue the hypoexcitability phenotype, we applied 100 nM of **α**-Dendrotoxin (**α**-DTX), and patched dPAG cells. Strikingly, when we applied the same current steps to *Setd5*$^{+/-}$ cells in the presence of the Kv blocker, the spiking activity was rescued to levels similar to *Setd5*$^{+/+}$ both before and after drug application (Fig. 5h-j). In addition, the spike dynamics remained identical in Setd5$^{+/+}$ after **α**-DTX application, whereas *Setd5*$^{+/-}$ became faster, mimicking the WT properties. These differences are not due to an overexpression of Kv1.1. Compared to other brain regions (Supplementary Fig. 10n-o), the dPAG seems to have a trend toward a reduction of the protein levels (Fig. 5l), while protein distribution is not affected (Fig. 5m-p). Kv1.1 has been recently shown to be involved in the homeostatic control of firing[27,28] through modulation of the axon initial segment (AIS)[29]. Thus, our behavioural and physiological results isolate a key molecular player in *Setd5*, Kv1.1, that causes the physiological hypoexcitability phenotype, probably arising through homeostatic misregulation, either by localisation[27], post-translational modifications[30] or interactions with auxiliary subunits[31].

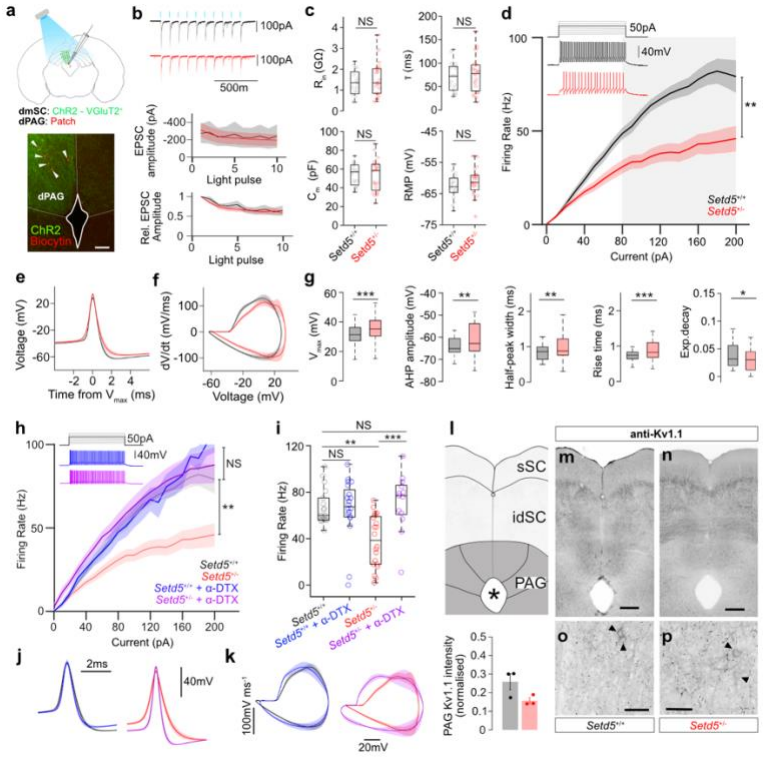

Figure 5. *Setd5*$^{+/-}$ dPAG cells are hypoexcitable due to misregulation of K_v channels. a, Schematic of the experimental approach, *in vitro* patch clamp recordings (top) and micrograph of VGluT2^{+} dmSC projections to the dPAG infected with AAV9-ires-DIO-ChR2 (green) with dPAG biocytin filled and recorded cells (arrows, scale bar: 100 **µ**m). **b**, Top, whole-cell voltage clamp traces of example *Setd5*$^{+/+}$ and *Setd5*$^{+/-}$ cells (black and red, respectively) responding to 10 Hz light stimulation. Amplitude (middle, p = 0.078) and relative EPSC amplitude (bottom, p = 0.565) of responses to sequential light pulses in a 10 Hz train. **c**, Box and whisker plots of the intrinsic response variables showing no significant difference in the input resistance (p = 0.688, top left), membrane constant tau (p = 0.654, top right), membrane capacitance (p = 0.668, bottom left) and resting membrane potential (p = 0.104, bottom right). **d**, Summary of the relationship between current-injection and action potential firing showing a strong reduction in firing (p < 0.001). Inset, representative example traces to a 50 pA current injection. **e**, Average shape and **(f)** phase plane analysis of the action potentials generated in the rheobase sweep (*Setd5*$^{+/+}$, 19 cells, 108 spikes; *Setd5*$^{+/-}$, 21 cells, 127 spikes). **g**, Summary of the action potential kinetics analysis. From left to right: action potential amplitude (V_{max}) (P < 0.001); after-hyperpolarisation (AHP) amplitude (P = 0.001), width at half-peak (P = 0.010), action potential rise time (P < 0.001) and exponential decay constant (P = 0.032). **h**, Same as (**d**) but also for *Setd5*$^{+/+}$ (blue) and *Setd5*$^{+/-}$ (purple) in the presence of **α**-Dendrotoxin, a Kv1.1, 1.2 and 1.6 blocker (**α**-DTX, 100 nM), (p > 0.995 and p = 0.0147 for the effect of **α**-DTX on *Setd5*$^{+/+}$ and *Setd5*$^{+/-}$ firing, respectively). **I**, Box and whisker plot of the firing rate to 120 pA current-injections (*Setd5*$^{+/+}$ without **α**-DTX, black, 63.3±15.3 Hz, n = 18; *Setd5*$^{+/+}$ with **α**-DTX, blue, 66.9±28.5 Hz, n = 20; *Setd5*$^{+/-}$ without **α**-DTX, red, 38.0±22.5 Hz, n = 20; *Setd5*$^{+/-}$ with **α**-DTX, purple, 71.5 ± 24.7 Hz, n = 13). **j**, Action potential shape and **k**, phase plane analysis of the action potentials generated in the rheobase current in *Setd5*$^{+/+}$ cells (without **α**-DTX, black, n =19; with **α**-DTX, blue, n =12), *Setd5*$^{+/-}$ cells (without **α**-DTX, red, n=21; with **α**DTX, purple, n = 13). **l**, top, schematic of SC and PAG regions of interest. Bottom, Western blot analysis of Kv1.1 protein content within the PAG of *Setd5*$^{+/+}$ (n = 3, 0.259) and *Setd5*$^{+/-}$ mice (n = 3, 0.157, P = 0.090). **m-p**, Antibody staining for Kv1.1 in Setd5$^{+/+}$ (**m**, 55 µm projection; **o**, 30 µm projection) and Setd5$^{+/-}$ (**n**, 55 µm projection; **p**, 30 µm projection). Arrowheads indicate somas stained for Kv1.1. Scale bar: **m**, **n:** 50 µm; **o**, **p**: 200 µm. Lines and shaded areas, mean ± s.e.m., respectively. P-values are Wilcoxon's rank sum test. p-values are two-way repeated measures ANOVA. For detailed statistics, see Supplementary Table 1.

The convergent nature of our behaviour across ASD models suggests that a dPAG hypoexcitability phenotype might be a widespread mechanism, occurring beyond *Setd5*. To test this possibility, we recorded from dPAG

neurons in *Ptchd1* and *Cul3* animals. These experiments revealed that *Ptchd1* animals, despite having mostly identical intrinsic properties (Fig. 6a), also show a hypoexcitability phenotype at high current inputs (Fig. 6b-d). Contrary to *Setd5*, this phenotype was not rescued by **α**-DTX application, showing that similar physiological phenotypes can arise from distinct molecular mechanisms (Fig. 6b). In contrast to these physiological phenotypes, *Cul3* animals did not show any changes in neither their current-firing relationship nor intrinsic properties (Fig. 6e-h).

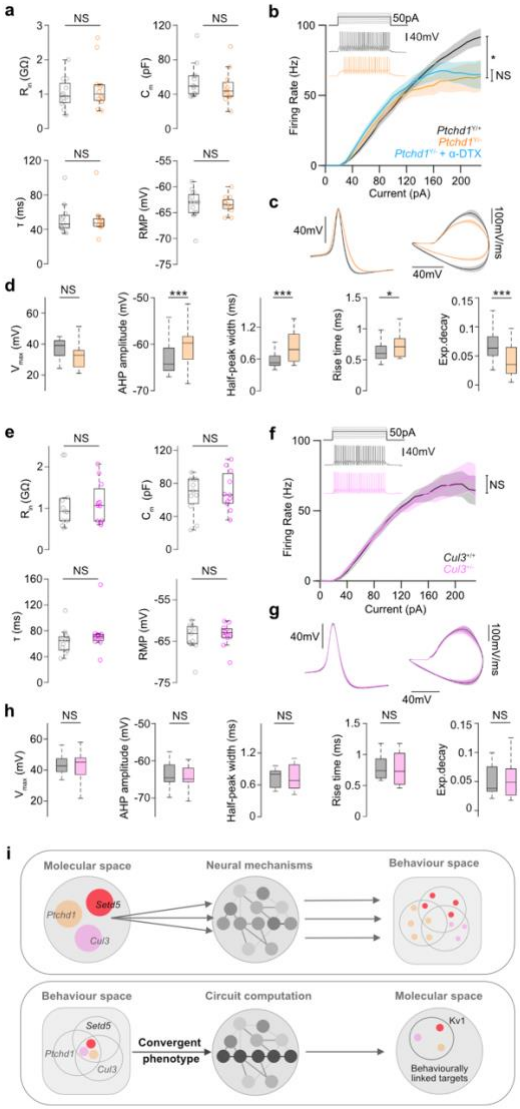

Figure 6. Electrophysiological characterisation of dPAG cells in *Ptchd1* and *Cul3* models reveals distinct molecular and circuit mechanisms behind conserved decision-making delay. a, Intrinsic response properties: input resistance ($p = 0.623$, top left), membrane capacitance ($p = 0.299$, top right), membrane constant tau ($p = 0.795$, bottom left) and resting membrane potential ($p = 0.749$, bottom right). **b**, Summary of the relationship between current-injection and action potential firing showing a strong reduction in firing (Effect of genotype without **α**-DTX: $p = 0.046$; effect of **α**-DTX on *Ptchd1*$^{Y/-}$ firing: $p = 0.680$). Inset, representative example traces to a 50 pA current injection for *Ptchd1*$^{Y/+}$ (black, top) and *Ptchd1*$^{Y/-}$ (orange, bottom). **c**, Average shape (left) and phase plane analysis (right) of the action potentials generated in the rheobase sweep (*Ptchd1*$^{Y/+}$, 16 cells, 58 spikes; *Ptchd1*$^{Y/-}$, 20 cells, 72 spikes). **d**, Summary of the action potential kinetics analysis for the *Ptchd1* model. From left to right: action potential amplitude (V_{max}) ($P = 0.092$); after-hyperpolarisation (AHP) amplitude ($P < 0.001$), width at half-peak ($P < 0.001$), action potential rise time ($P = 0.011$) and exponential decay

constant (P < 0.001). **e**, as for **a** but for *Cul3*$^{+/+}$ (grey) and *Cul3*$^{+/-}$ (pink) dPAG cells. Input resistance (p = 0.896, top left), membrane capacitance (p = 0.896, top right), membrane constant tau (p = 0.212, bottom left) and resting membrane potential (p = 0.844, bottom right). **f**, as for **b** but for *Cul3*$^{+/+}$ (grey, 12 cells, n = 3) and *Cul3*$^{+/-}$ (pink, 12 cells, n = 3, p = 0.683 for the effect of genotype). **g**, as for **c** but *Cul3*$^{+/+}$ (grey, 68 spikes) and *Cul3*$^{+/-}$ (pink, 73 spikes). **h**, Summary of the action potential kinetics analysis for the *Cul3* model. From left to right: action potential amplitude (V_{max}) (P = 0.984); after-hyperpolarisation (AHP) amplitude (P = 0.296), width at half-peak (P = 0.565), action potential rise time (P = 0.399) and exponential decay constant (P = 0.867). **i**, Schematic representing the approaches used to studying brain disorders. Classically, the effects of molecular dysfunctions are studied independently across a palette of different neuronal mechanisms, with behaviour as a conclusive remark (top). We focus on behaviour first. By defining a convergent dysfunction, we directly constrain the underlying neuronal circuit across models, enabling a comparative understanding of the underlying molecular changes (bottom). Lines are shaded areas, mean ± s.e.m., respectively. P-values are Wilcoxon's rank sum test. p-values are two-way repeated measures ANOVA. For detailed statistics, see Supplementary Table 1.

Discussion

Autism spectrum disorders (ASDs) are widespread in the global population, but our understanding of the disorder's origins remains limited. Advancements in genetic sequencing technologies have enabled the isolation of autism-risk genes, opening the door to several in-depth studies into the molecular mechanism of action of these genes[32]. However, there is a considerable mismatch between the observed wealth of molecular changes and our understanding of their roles in appropriate circuit function and, therefore, behaviour. Thus, direct comparisons across models have been difficult, leading to studies focusing on single models, defining particular changes but not general principles[33]. Here we show that the study of innate defensive behaviours provides a convergent behavioural framework that enables the directed analysis of the underlying sensorimotor processes up to the molecular level, permitting comparative dissections of the neuronal dysfunctions across ASD models. Our approach is inspired by David Marr's three levels analysis[34], a systems-level approach to understanding complex systems[35]. Contrary to the classical strategies to study mental disorders that start at the molecular level, we flipped the approach to find and focus on a convergent behavioural dysfunction (Fig. 6i). This defined a common pathological computation, an inappropriate interaction with the environment (Marr's level 1), and narrowed down the algorithmic problem, subcortical visuomotor processing (Marr's level 2). By doing so, we standardised the understanding of the different molecular and circuit-level implementations (Marr's level 3) that underly the behavioural dysfunction.

Defensive escape behaviours are among the most basal perceptual decisions performed by animals[18]. Their finely-tuned mechanisms are indispensable for survival, but also for properly interacting with the environment. Whereas some stimuli unambiguously signal an imminent threat and should instruct immediate action, others are ambiguous and require adaptive responses arbitrated by the current context and state to decide, e.g., between ignoring, freezing, fighting, or escaping[18]. In mice, behavioural escape decisions are known to be initiated by the dPAG[24], where appropriate escape decisions are thought to be determined. While all tested ASD models can, in principle, respond behaviourally as robustly as their WT siblings, they require longer and respond with less vigour once an action has been initiated, hampering their ability to develop an appropriate place aversion to the threat zone (Figs. 1 & 2). The underlying changes were rigorously dissected in the *Setd5* haploinsufficient model, pointing to a specific misregulation of the voltage-gated potassium channel Kv1.1 in dPAG neurons that gives rise to a strong hypoexcitability phenotype (Fig. 5). Importantly, as argued before[35], the relevance of defining a concurrent node for the dissection of behaviourally relevant molecular changes becomes evident. Whereas *Ptchd1* dPAG neurons show a hypoexcitability phenotype, deficits in LAR are independent of dPAG intrinsic properties in *Cul3* (Fig. 6). These results are in line with a previous characterisation which demonstrated that thalamic reticular impairments in *Ptchd1* are linked to a reduction in the conductance of calcium-dependent potassium currents[21]. In contrast, deficits in cytoskeleton protein homeostasis and cell migration abnormalities

have been described in *Cul3* animals[20]. Thus, despite similar behavioural phenotypes, the molecular causes diverge, reflective of the described molecular complexity of ASD. Furthermore, the behavioural and physiological phenotypes are tightly linked. Substantial threat evidence, either by strong optogenetic activation of dmSC neurons or high-contrast visual looms, elicit a slower and less robust response in *Setd5*$^{+/-}$ compared to their WT siblings. On the other hand, limited threat evidence, either by weak optogenetic activation or low-contrast looms, instructs similar behavioural responses between genotypes (Fig. 4). Accordingly, only strong current-injections that match the expected dPAG drive caused by high contrast loom[24] cause a hypoexcitability phenotype, indicating that the delayed response phenotype is due to a dPAG dysfunction. This stimulus strength relationship aligns with the coping difficulties of many individuals with ASD to salient sensory stimuli, such as bright lights or crowded places, but not to mellow sensory environments[8]. Interestingly, the involvement of voltage-gated potassium channels in the generation of proper perceptual decisions appears to be a widespread principle across the animal kingdom, as recently shown in *Drosophila*[36].

The link between potassium channels and autism is well established. Genetic analyses of individuals with ASD uncovered deleterious mutations in potassium channels[37]. These, however, exclude Kv1.1. Interestingly, autistic-like repetitive and social behaviours in the *Scn2a* haploinsufficiency mouse model have been rescued in a Kv1.1 deficient background[38], supporting our results that enhancing and not disrupting Kv1.1's contribution through homeostatic misregulation can be a fundamental factor in ASD. This makes one wonder why LAR would require homeostatic control in the first place. Kv1.1 is implicated with rapid, <10 min, homeostatic regulation of hippocampal excitability[27,28]. Recently, it has been shown that LAR can be flexibly controlled in timeframes <10 min, suppressing the LAR completely by sensitising a threat memory[26]. This timeframe matches our results (Fig. 2n-p), suggesting that Kv1.1 regulation might be one of the mechanisms underlying the learned suppression of escape. Thus, we speculate that Kv1.1 homeostatic control is a common denominator regulating the appropriate strength of responsiveness to threat stimuli, causing abnormal behaviour when misregulated, as shown in *Setd5*$^{+/-}$ animals.

The repetitive LAR phenotype is associated with a reduction in place aversion to the threat zone and suggests that ASD mouse models are either less fearful or incapable of interpreting the noxiousness of threat experience appropriately (Figs. 1 & 2, Supplementary Figs. 1j,k & 2j,k), a maladaptive behaviour that recapitulates some human ASD traits[39]. Interestingly, this reduction of place aversion is directly linked with longer reaction times to the LAR, and thus, with the dPAG hypoexcitability phenotype (Fig. 2i,j). This suggests that maladaptive perceptual decisions, as with the delayed LAR, can have a profound effect on seemingly independent behavioural properties. Although our results show that the excitability effects are not global but area-specific (Fig. 5, Supplementary Fig. 10), alternatively, other brain areas could also be involved, e.g., the lateral amygdala or the lateral posterior thalamus (LP)[40].

The diagnostic criteria for autism are behavioural and are mainly focused on abnormal social interactions, communication deficits, and repetitive behaviours. Thus, in animal models, a strong focus has been devoted to the generation of a comprehensive set of assays for these abnormal behaviours as tools for discovering effective treatments[41]. Progress in ASD research, however, is limited by the lack of clear and robust behaviours, whose alterations can be mapped causally at a circuit level. Although directly relevant to ASD, the inherent complexity of the behaviours that match the classical ASD criteria makes them tremendously difficult to dissect at a systems level. Innate behaviours like the LAR, on the other hand, provide an orthogonal avenue to bridge quantifiable behavioural abnormalities to a circuit- and molecular-level understanding of the disorder, as done here for *Setd5*. Our behavioural and circuit-level understanding of innate visually-guided defensive responses, provides a quantitative framework to systematically link behavioural metrics with the relevant molecular changes, and thus, may reveal therapeutic targets as envisioned by precision medicine approaches in autism[32].

References and Notes

1. Baron-Cohen, S., Leslie, A. M. & Frith, U. Does the autistic child have a "theory of mind"? *Cognition* **21**, 37–46 (1985).
2. Tomchek, S. D. & Dunn, W. Sensory processing in children with and without autism: a comparative study using the short sensory profile. *Am. J. Occup. Ther.* **61**, 190–200 (2007).
3. Pelphrey, K. A., Shultz, S., Hudac, C. M. & Vander Wyk, B. C. Research review: Constraining heterogeneity: the social brain and its development in autism spectrum disorder. *J. Child Psychol. Psychiatry* **52**, 631–644 (2011).
4. Buckner, R. L., Andrews-Hanna, J. R. & Schacter, D. L. The brain's default network: anatomy, function, and relevance to disease. *Ann. N. Y. Acad. Sci.* **1124**, 1–38 (2008).
5. Minshew, N. J. & Williams, D. L. The new neurobiology of autism: cortex, connectivity, and neuronal organization. *Arch. Neurol.* **64**, 945–950 (2007).
6. Robertson, C. E. & Baron-Cohen, S. Sensory perception in autism. *Nat. Rev. Neurosci.* **18**, 671–684 (2017).
7. Simmons, D. R. *et al.* Vision in autism spectrum disorders. *Vision Res.* **49**, 2705–2739 (2009).
8. McFadyen, J., Dolan, R. J. & Garrido, M. I. The influence of subcortical shortcuts on disordered sensory and cognitive processing. *Nat. Rev. Neurosci.* **21**, 264–276 (2020).
9. Kleinhans, N. M. *et al.* fMRI evidence of neural abnormalities in the subcortical face processing system in ASD. *Neuroimage* **54**, 697–704 (2011).
10. Hadjikhani, N. *et al.* Look me in the eyes: constraining gaze in the eye-region provokes abnormally high subcortical activation in autism. *Sci. Rep.* **7**, 3163 (2017).
11. Hu, Y. *et al.* A translational study on looming-evoked defensive response and the underlying subcortical pathway in autism. *Sci. Rep.* **7**, 14755 (2017).
12. Jones, W. & Klin, A. Attention to eyes is present but in decline in 2–6-month-old infants later diagnosed with autism. *Nature* vol. 504 427–431 at https://doi.org/10.1038/nature12715 (2013).
13. Volkmar, F. R., Lord, C., Bailey, A., Schultz, R. T. & Klin, A. Autism and pervasive developmental disorders. *J. Child Psychol. Psychiatry* **45**, 135–170 (2004).
14. Madipakkam, A. R., Rothkirch, M., Dziobek, I. & Sterzer, P. Unconscious avoidance of eye contact in autism spectrum disorder. *Sci. Rep.* **7**, 13378 (2017).
15. Tokuoka, K., Kasai, M., Kobayashi, K. & Isa, T. Anatomical and electrophysiological analysis of cholinergic inputs from the parabigeminal nucleus to the superficial superior colliculus. *J. Neurophysiol.* **124**, 1968–1985 (2020).
16. Jure, R. Autism Pathogenesis: The Superior Colliculus. *Front. Neurosci.* **12**, 1029 (2018).
17. Yilmaz, M. & Meister, M. Rapid innate defensive responses of mice to looming visual stimuli. *Curr. Biol.* **23**, 2011–2015 (2013).
18. Branco, T. & Redgrave, P. The Neural Basis of Escape Behavior in Vertebrates. *Annu. Rev. Neurosci.* **43**, 417–439 (2020).
19. Deliu, E. *et al.* Haploinsufficiency of the intellectual disability gene SETD5 disturbs developmental gene expression and cognition. *Nat. Neurosci.* **21**, 1717–1727 (2018).
20. Morandell, J. *et al.* Cul3 regulates cytoskeleton protein homeostasis and cell migration during a critical window of brain development. *Nat. Commun.* **12**, 1–22 (2021).
21. Wells, M. F., Wimmer, R. D., Schmitt, L. I., Feng, G. & Halassa, M. M. Thalamic reticular impairment underlies attention deficit in Ptchd1Y/− mice. *Nature* **532**, 58–63 (2016).
22. Bandler, R., Depaulis, A. & Vergnes, M. Identification of midbrain neurones mediating defensive behaviour in the rat by microinjections of excitatory amino acids. *Behav. Brain Res.* **15**, 107–119 (1985).
23. Deng, H., Xiao, X. & Wang, Z. Periaqueductal Grey Neuronal Activities Underlie Different Aspects of Defensive Behaviors. *J. Neurosci.* **36**, 7580–7588 (2016).
24. Evans, D. A. *et al.* A synaptic threshold mechanism for computing escape decisions. *Nature* **558**, 590–594 (2018).
25. Zhao, X., Liu, M. & Cang, J. Visual cortex modulates the magnitude but not the selectivity of looming-evoked

responses in the superior colliculus of awake mice. *Neuron* **84**, 202–213 (2014).
26. Lenzi, S. C. *et al.* Threat history controls flexible escape behavior in mice. *Curr. Biol.* **0**, (2022).
27. Zbili, M. *et al.* Homeostatic regulation of axonal Kv1.1 channels accounts for both synaptic and intrinsic modifications in the hippocampal CA3 circuit. *Proc. Natl. Acad. Sci. U. S. A.* **118**, (2021).
28. Morgan, P. J., Bourboulou, R., Filippi, C., Koenig-Gambini, J. & Epsztein, J. Kv1.1 contributes to a rapid homeostatic plasticity of intrinsic excitability in CA1 pyramidal neurons in vivo. *Elife* **8**, (2019).
29. Grubb, M. S. & Burrone, J. Activity-dependent relocation of the axon initial segment fine-tunes neuronal excitability. *Nature* **465**, 1070–1074 (2010).
30. Winklhofer, M. *et al.* Analysis of phosphorylation-dependent modulation of Kv1.1 potassium channels. *Neuropharmacology* **44**, 829–842 (2003).
31. Niespodziany, I. *et al.* Discovery of a small molecule modulator of the Kv1.1/Kvβ1 channel complex that reduces neuronal excitability and in vitro epileptiform activity. *CNS Neurosci. Ther.* **25**, 442–451 (2019).
32. Kostic, A. & Buxbaum, J. D. The promise of precision medicine in autism. *Neuron* **109**, 2212–2215 (2021).
33. Willsey, H. R., Willsey, A. J., Wang, B. & State, M. W. Genomics, convergent neuroscience and progress in understanding autism spectrum disorder. *Nat. Rev. Neurosci.* **23**, 323–341 (2022).
34. Marr, D. *Vision*. (MIT Press, 2010).
35. Krakauer, J. W., Ghazanfar, A. A., Gomez-Marin, A., MacIver, M. A. & Poeppel, D. Neuroscience needs behavior: Correcting a reductionist bias. *Neuron* **93**, 480–490 (2017).
36. Groschner, L. N., Chan Wah Hak, L., Bogacz, R., DasGupta, S. & Miesenböck, G. Dendritic Integration of Sensory Evidence in Perceptual Decision-Making. *Cell* **173**, 894-905.e13 (2018).
37. Guglielmi, L. *et al.* Update on the implication of potassium channels in autism: K+ channelautism spectrum disorder. *Front. Cell. Neurosci.* **9**, (2015).
38. Indumathy, J., Pruitt, A., Gautier, N. M., Crane, K. & Glasscock, E. Kv1.1 deficiency alters repetitive and social behaviors in mice and rescues autistic-like behaviors due to Scn2a haploinsufficiency. *Brain Behav.* **11**, e02041 (2021).
39. Macari, S. *et al.* Emotional Expressivity in Toddlers With Autism Spectrum Disorder. *J. Am. Acad. Child Adolesc. Psychiatry* **57**, 828-836.e2 (2018).
40. Wei, P. *et al.* Processing of visually evoked innate fear by a non-canonical thalamic pathway. *Nat. Commun.* **6**, 6756 (2015).
41. Silverman, J. L., Yang, M., Lord, C. & Crawley, J. N. Behavioural phenotyping assays for mouse models of autism. *Nat. Rev. Neurosci.* **11**, 490–502 (2010).
42. Yang, H., Wang, H. & Jaenisch, R. Generating genetically modified mice using CRISPR/Cas-mediated genome engineering. *Nat. Protoc.* **9**, 1956–1968 (2014).
43. Brainard, D. H. The Psychophysics Toolbox. *Spat. Vis.* **10**, 433–436 (1997).
44. Gupta, D., Młynarski, W., Symonova, O., Svatoň, J. & Joesch, M. Panoramic visual statistics shape retina-wide organization of receptive fields. *bioRxiv* 2022.01.11.475815 (2022) doi:10.1101/2022.01.11.475815.
45. Pachitariu, Steinmetz & Kadir. Fast and accurate spike sorting of high-channel count probes with KiloSort. *Adv. Neural Inf. Process. Syst.*
46. Lee, K. H., Tran, A., Turan, Z. & Meister, M. The sifting of visual information in the superior colliculus. *Elife* **9**, (2020).
47. Stitt, I., Galindo-Leon, E., Pieper, F., Engler, G. & Engel, A. K. Laminar profile of visual response properties in ferret superior colliculus. *J. Neurophysiol.* **110**, 1333–1345 (2013).
48. Montijn, J. S. *et al.* ZETA: a parameter-free statistical test for neuronal responsiveness. *bioRxiv* 2020.09.24.311118 (2021) doi:10.1101/2020.09.24.311118.
49. Mathis, A. *et al.* DeepLabCut: markerless pose estimation of user-defined body parts with deep learning. *Nat. Neurosci.* **21**, 1281–1289 (2018).

Acknowledgments

We thank Prof. Peter Jonas for his suggestion on the involvement of potassium channels and members of the Neuroethology group for their comments on the manuscript. Katalin Szigeti and Julie Murmann for experimental help. This research was supported by the Scientific Service Units of IST Austria through resources provided by the Lab Support Facility, the Imaging and Optics Facility, the Machine Shop Unit and the Preclinical Facility, especially Freyja Langer and Michael Schunn. This work was supported by European Research Council Starting Grant 756502 (MJ).

Author contributions

LB and MJ designed the study. LB analysed all data with help from OS. LB performed the behavioural, optogenetic and *in vivo* electrophysiology experiments with help from TVZ. PK performed the *in vitro* experiments. LB, MJ and OS developed the behavioural system and analysis pipeline. TVZ, OS and MJ developed the *in vivo* electrophysiology setup and LB the analysis pipeline. TM performed the protein level analysis. XC, GN and TR generated the *Ptchd1* mouse line. GN and RS provided mouse lines, reagents and gave advice on the study design. LB and MJ wrote the manuscript with help of the other authors.

Competing interests

Authors declare that they have no competing interests.

Data availability

All data used in the analysis will be made available at IST DataRep upon publication.

Code availability

All code used to generate the results will be made available at Github upon publication.

Methods

Mice

The study was discussed and approved by the institutional ethics committee of the University of Veterinary Medicine Vienna and the Institute of Science and Technology Austria in accordance with good scientific practice guidelines and national legislation under license numbers BMWF-68.205/0023-II/3b/2014 and 66.018/0017-WF/V/3b/2017. Male and female adult *Setd5*$^{+/-}$, *Setd5*$^{+/fl}$::*Emx1*-Cre, *Setd5*$^{+/-}$::*VGluT2*-ires-Cre, *Cul3*$^{+/-}$, *Ptchd1*$^{Y/-}$ mice were housed under a 12h light/dark cycle (lights on at 07:00), with food and water available ad libitum. The animals were housed in groups of 2-6 animals per cage and were tested during the light phase. Animals used for the *in vivo* electrophysiological recordings or freely-moving optogenetics experiments were group housed before surgery and individually housed after the surgery. Mice were chosen based on genotypes. Sex-matched animal pairs of control-mutant siblings from the same litters were compared to decrease variance due to age, environment and genetic background. For the number and sex of animals used in the experiments, please refer to Supplementary Table 1.

Generation of Ptchd1$^{Y/-}$ mice

Ptchd1$^{Y/-}$ mice for analysis were generated using the CRISPR/Cas9 system, as described in [42]. In brief, *in vitro* transcribed sgRNAs targeting the exon 2 of *Ptchd1* were microinjected into zygotes of C57BL/6NRj mice together with Cas9 *mRNA*. Offspring were screened by PCR for deletions using primers spanning the target sites (5′-GTAGGGCTGGAATCATGAGG-3′, 5′-CACATCCTTTGGTGTGATGC-3′). Deletion of *Ptchd1* exon 2 was confirmed by Sanger sequencing analyses. The founder line was established from a female *Ptchd1*$^{+/-}$ mouse with a 1.26 kb deletion. Analysis of *Ptchd1* transcript level by RT-PCR confirmed impaired *Ptchd1* expression in brain, cerebellum and kidney of the *Ptchd1*$^{Y/-}$ mice, compared to control mice.

Behavioural procedures

Experimental setup. All behavioural experiments were performed at mesopic light levels, in a square, black, IR-transparent Perspex box (W: 32 cm x L: 32 cm x H: 32 cm) with a shelter made of the same material (9 cm x 9 cm x 3 cm) positioned in one corner. One wall of the box was 2 cm shorter to allow for ventilation and for the optic fibre to pass through for optogenetic experiments. A plastic screen covered with a plastic sheet with a matte surface was placed as a lid on top of the box, and a modified Texas Instruments DLP projector (DLP CR4500EVM) back-projected a grey background. The blue LED was exchanged for a high-power UV-LED (ProLight 1W UV LED, peak 405 nm) to improve the differential stimulation of S pigments. The experiments were recorded with a near-IR camera (acA1920-150um, Basler, 60 Hz) from below the centre of the arena. Video recording, visual and optogenetic stimulation were controlled using custom software written in MATLAB, python and arduino. The entire apparatus was housed within a sound-deadening, light-proof cabinet which was illuminated by an infrared light-emitting diode (LED) lamp (SIL 616.21, Sanitas).

Protocols. All animals were habituated to the test arena at least one day before testing and were allowed to explore the arena for at least 20 mins. The initial 10 min of this exploration time was recorded and used to analyse the animals' exploratory behaviour (Supplementary Fig.5). For the looming avoidance response (LAR: Figs.1, 2, S1, S2, S3, S4, S6) paradigm, responses were tested over five consecutive days. On each test day the animals were given 10 min to acclimatise to the arena, after which they were subjected to 3 test trials, with a 3 min interval between each trial. Each trial lasted 180 s, within which the central position of the mouse was tracked online (Python) and was used to trigger the visual stimuli in a closed-loop manner whenever the mouse crossed a designated threshold distance (10 cm) from the centre of the shelter, with a minimum stimulus interval of 30 s. A typical experiment lasted ~30 min and the entire arena was cleaned with 70 % ethanol between animals.

In preparation for the reward trials, after the 4th day of testing a small piece of banana chip was placed in the opposite corner of the arena to the shelter and the mice were free to explore the arena without triggering any loom stimuli. The animals were left to explore until they successfully acquired the banana chip, after which time both the mouse and the chip were placed back in their home cage. The reward trial then took place after the 5th day of testing. Another small piece of banana chip was again placed in the opposite corner of the arena and the animals were free to explore, however this time whenever the mouse passed the threshold distance from the shelter a looming stimulus would start, this time with no inter-stimulus interval. For different contrast experiments, animals were presented with looming stimuli of 20, 50 or 98 % contrast in a pseudorandom order upon crossing the trigger threshold. The background luminosity remained constant while the luminance of the disc was increased to generate low contrast stimuli.

Learned suppression of escape (LSE) experiments (Fig. 2m-p) were conducted as in[26]. Naive mice were habituated to the arena for 10 min before the shelter was removed from the arena and a series of 8 blocks of 3 loom stimuli were presented to the mice with 40 s intervals. The luminance of the black disc remained constant but the luminosity of the background increased with each block and for the preceding 40 s period. Once all the looms had been presented, the shelter was returned to the arena and the mice were given an additional 7 min in the arena before they were tested with the standard high contrast loom stimuli.

Visual Stimuli. Stimuli were created and presented using custom-made scripts in MATLAB (MathWorks, Inc.), using the Psychophysics Toolbox extensions[43]. The standard stimulus consisted of a dark disc on a grey background presented on the lid over the centre of the arena, that reached a maximum size of 40 deg/visual angle. The disc expanded over 500 ms at a speed of 80 deg s^{-1} and then remained at this size for 250 ms before disappearing and a new expanding disc immediately appearing. A maximum of 5 expanding discs were shown in a single loom bout. A red rectangle was presented along one side of the projected image every 5th frame, onto an out-of-view section of the arena lid. An optical filter reflected this red light back towards a photodiode (PDA36A2, ThorLabs) and this information was then used for post-hoc synchronisation of the behavioural data and the stimulus.

Analysis. Automatic image processing of the behavioural video frames identified the central position of the mouse and the heading direction. Exploratory behavioural metrics during the acclimatisation period were calculated from videos of the first 10 min mice were placed within the arena. A shelter exit was defined as an episode where the full body of the mouse moved from the inside to the outside of the shelter. The maximum distance travelled during an exit was defined as the maximal distance reached in a straight line between the centre of the mouse and the centre of the shelter. The exit duration was defined as the time between when the full body of the mouse crossed over until it re-crossed the shelter boundary. The interbout interval during exploration was the time between subsequent shelter exits. The centre position of the mouse, $[X_m, Y_m]$, was used to quantify the percentage of the 10 min recorded that the mouse was either outside of the shelter, in the centre of the area (defined as a circular area, centred on the centre of the arena where the loom was presented, $[X_c, Y_c]$, with a 7 cm radius) or at the edge of the area (defined as outside of a circular area, centred on $[X_c, Y_c]$ with a 14 cm radius).

LAR responses were assessed by analysing a peri-stimulus period starting from 3 s before the stimulus until 10 s after the stimulus onset. Responses were classified as escapes if the mouse returned to the shelter within 7 s after stimulus onset and reached a maximum speed of >20 cm s^{-1} in travelling back to the shelter. The maximum escape speed was calculated as the peak value of the speed trace between the onset of the escape and entry into the shelter. The reaction time of the mouse was calculated as the time from stimulus onset till the mouse reached the maximum speed during its escape back to the shelter. This reaction time was then used to group the responses of the animals (Figs. 1c, S1b, S2b, S3b, S6b) depending on which loom presentation the peak of their escape response was recorded. The number of looms triggered is the total number of loom stimuli triggered across the

5 days of testing, not including the reward trial. The Log_{10}(**Δ**Speed) (Fig. 1i-k, S3e, S6e) was calculated as the logarithmic of the ratio between the average speed in the time 300-800 ms after the start of the stimulus and the average speed in the peristimulus period ±50 ms around the start of the stimulus.

To understand the effect of certain parameters of the mouse's position and location within the arena on its LAR response we calculated the distance of the mouse from shelter (defined as the straight line distance between [X_m, Y_m] and [X_s, Y_s]) and the heading angle of the mouse at the time of stimulus start (defined as the angle (BÂC) between point B, the tip of the mouse's snout, A, the position between the two back paws of the mouse and C the centre of the shelter, [X_s,Y_s]). The position of the mouse's body parts was located using DeepLabCut tracking[41]. The trajectory directedness of individual escapes was defined as (1 - (d-d_{min}/d+d_{min})), where d is the cumulative displacement of the mouse from its position at the time of the stimulus, [X_m,Y_m], start till when the centre of the mouse's body re-enters the shelter, and d_{min} is the straight line distance between [X_m, Y_m] and [X_s, Y_s]. The distance from the loom was calculated as the straight distance between the centre of the arena [X_c, Y_c], and the centre of the mouse [X_m, Y_m].

For the analysis of the response dynamics during the reward trials, only trials where the animals made a noticeable escape back to the shelter were included. Four *Setd5*$^{+/-}$ trials were removed from the final analysis because the mouse was interacting with the banana chip reward during the stimulus presentation.

For the behavioural experiments, the initial tracking and analysis of the escape behaviour were done blind through automatic analysis scripts and the genotypes were added later when pooling the animal's data together. Behaviour metrics were calculated both by pooling trials across all animals and also by calculating the average per mouse and computing an average across all mice, detailed explanations of each analysis can be found in Supplementary Table 1 and are mentioned specifically in the text.

Viruses

The viruses used in this study: for optogenetic activation, adeno-associated virus (AAV) AAV9-EF1a-DIO-hChR2(E123T)T159C)-EYFP-WPRE-hGH (1×10^{13} viral genomes per ml (vg ml^{-1}), Addgene 35509); for control experiments, AAV9-Syn-Flex-GCaMP6m-WPRE-SV40 (1×10^{13} vg/ml, Addgene 100838).

Surgical procedures

Mice were anaesthetised with an intraperitoneal (i.p.) injection of ketamine (95 mg kg^{-1}) and xylazine (4.5 mg kg^{-1}), followed by metamizol (20 mg kg^{-1}, i.p.) and buprenorphine (0.05 mg kg^{-1}, i.p.) and meloxicam (2 mg kg^{-1}, subcutaneous (s.c.)). If needed, isoflurane (0.5-2 % in oxygen, 0.8 l min^{-1}) was used to maintain anaesthesia. Fur on the top of the head was removed with an electric hair remover (Braun Precision Trimmer, PT 5010) then the mice were placed in a stereotaxic frame (Model 962, Kopf Instruments) and fixed using the ear bars. Eyes were protected using Oleo Vital eye cream and a topical analgesic (Xylocain 2 % gel) was applied to the skin with a q-tip before cutting the skin. Craniotomies of were made using 0.5 mm burrs (Fine Science Tools) and dental drill (Foredom, HP4-917) and viral vectors were delivered using pulled pipettes (World Precision Instruments, 1.4 mm OD, 0.53 mm ID, #504949) made with a micropipette puller (DMZ Zeitz-puller, Germany) and delivered using an automatic nanoinjector (World Precision Instruments, Nanoliter 2010) at 20 nl min^{-1}. The skin was closed after surgery using surgical glue (Vetbond, 3M, #1469SB).

Optogenetics experiments

Surgical procedure. Setd5$^{+/+}$::VGluT2-ires-Cre and Setd5$^{+/-}$::VGluT2-ires-Cre sex-matched sibling mice were injected with AAV9-DIO-ChR2-eYFP (see Viruses) into the right dmSC (75-100 nl, ML: -0.5, AP: -0.5 to -0.7, DV: -1.45 to -1.6, from bregma). Control mice were injected with 100nl of AAV9-Flex-GCaMP6m into the right dmSC at the same coordinates. One optic fibre (400 μm diameter, CFMC54L02, ThorLabs) was implanted 250 μm dorsal to the injection site. Fibres were affixed using light-curing glue (Optibond Universal, Kerr Dental)

and dental cement (SuperBond C&B Kit, Hentschel-Dental) and the skin was closed around the implant with surgical glue (Vetbond, 3M, #1469SB).

Experimental paradigm. The same behavioural arena was used for the optogenetic activation experiments except with the addition of a black piece of perspex (9 cm x 5 cm) positioned 10 cm above the floor in place of the closed shelter. Mice were similarly acclimatised to the arena, as in the LAR procedure, but with the fibre optic cable (200 μm, 0.48 NA, Doric Lenses) attached via a rotary joint (RJ1, ThorLabs) to allow for unrestrained movement and minimal handling of the animals. Since it has previously been shown[24] that increasing light intensity can be used as a proxy for the level of mSC, and hence dPAG, activation we decided to systematically modulate the laser light intensity in different trials. Once the trial began, mice were photostimulated (473 nm, 10 light pulses of 10 ms at 10 Hz; Shanghai Dream Lasers Technology) if they passed the threshold distance (10 cm) from the shelter, with a minimum inter-stimulus interval of 30 s. The initial laser intensity was set to a low irradiance (0.01-0.1 mW mm^{-2}) that did not evoke an observable behavioural response, however after at least 3 trials (180 s each, with a maximum 5 triggers per trial) at each intensity the irradiance was increased by (0.25-0.5 mW mm^{-2}). Laser power never exceeded 12 mW mm^{-2}. Two mice never elicited an observable escape behaviour, and post-processing histological analysis revealed mislocalised viral expression in these animals, and they were excluded from the analysis, along with their matched siblings.

Analysis. Trials were pooled across animals for each genotype and psychometric curves were generated by fitting logistic regression curves to the data. The data of the Log_{10}(**Δ**Speed) across laser powers was analysed using a two-way repeated measures ANOVA looking at the effect of genotype, laser power and their interaction, followed by a multiple comparisons analysis with Bonferroni correction. See Supplementary Table 1 for more details.

In vivo electrophysiology

Data acquisition. A 32-channel silicon probe (NeuroNexus, USA, A32-OM32) was used to record extracellular spikes from different depths of the SC in *Setd5*$^{+/+}$ (n = 3), *Setd5*$^{+/-}$ (n = 3), *Cul3*$^{+/+}$ (n = 3), *Cul3*$^{+/-}$ (n = 3), *Ptchd1*$^{Y/+}$ (n = 3) and *Ptchd1*$^{Y/-}$ (n = 3) sex-matched sibling mice. Mice were implanted with a custom-designed head plate over a ~0.5-1 mm diameter craniotomy (left hemisphere, AP: 0.4 to -0.4, ML: 0.4 to 0.8 from lambda) and a second craniotomy (~0.5 mm) was made anterior to bregma on the right hemisphere, where a reference gold pin was implanted and lowered until it touched the brain surface. Both were cemented to the skull using light-curing glue (Optibond Universal, Kerr Dental) and dental cement (SuperBond C&B Kit, Hentschel-Dental), with the headplate additionally fixed using Charisma Flow (Kulzer GmBH). The craniotomy was covered with Kwik-Cast (World Precision Instruments) to protect the underlying tissue before recording. At least 24 hrs after surgery, mice were placed on a suspended spherical treadmill (20 cm diameter) and head-fixed within a toroidal screen covering 190 ^{o} of visual angle which was illuminated by a DLP-light projector (Blue LED exchanged for UV 405 nm, 60 Hz) reflecting off a spherical mirror in front of the screen (see diagram in Fig. 3a). The behaviour of the animal was recorded by a near-IR camera (Basler, acA1920-150um, 30 Hz) from the reflection of the animal in an IR-reflective heat mirror positioned 30 cm from the face of the mouse and 35 cm from the camera. Prior to recording, the probe was coated with DiI (1 mM in ethanol, Merck, #42364) for later histological confirmation of the recording site and a wire was connected to the ground pin for both an external reference and ground. The kwik-cast seal was removed, revealing the brain surface and the confluence of the overlying superior sagittal and the left transverse sinus. Care was taken to position the probe as posteriorly and as medially as possible without damaging the sinuses or other blood vessels. It was then lowered, zeroed at the brain surface then slowly lowered into the overlying cortex and the SC at 1 mm s^{-1} to depths between 1.2-2.2 mm. The recording was started 15 min after reaching the desired depth to allow for stabilisation. The probe was lowered to 3-4 depths per animal with 250 μm intervals, to sample from cells across the depth of the SC.

Each recording took ~30 min, with the animal in the setup for ~180 min in total. Data was recorded at 20 kHz (PCIe-6321, National instruments and Intan board RHD2000 Evaluation Board version 1.0).

Visual Stimuli (*in vivo* electrophysiology)

Sensory stimuli were made using the Psychophysics Toolbox extensions in MATLAB (MathWorks, Inc.) and presented and synchronised using custom-made LabVIEW software. Frames were presented at a refresh rate of 60 Hz. At each depth, the mice were exposed to one 20 min presentation of a full field shifting spatiotemporal white-noise stimulus (see [44]) in order to assess receptive fields, and two repetitions of the remaining stimuli (5 x loom bouts, moving bars, moving gratings, full field flash). Each presentation would start with a uniform grey screen (60 s, green and UV LED intensities were set to match the sun spectrum from a mouse opsin perspective), followed by the first presentation of the looming stimulus, then the other stimuli in a pseudorandom order separated by 30 s gaps of a grey screen. White-noise "checker" stimuli were presented at 20 Hz update for 10 min. The checker size was 6.56 deg^2 and the entire grid was shifted between 0 and 3.25 deg in both x- and y-axis after every frame. Auditory monitoring of responses to a flashing point stimulus was used in real-time to gauge the rough centre of the receptive fields of the neurons being recorded and the location of the looming stimulus was positioned to overlap with this position. The looming stimulus consisted of 10 repetitions of 5 sequential, individual looming stimuli (a loom bout), as previously described in the behavioural experiments. These loom bouts would be presented with intervals of pseudorandom lengths between 10-30 s with a grey screen in between. To assess direction selectivity, the mice were presented with full-filed moving square gratings (1.5 cycles s^{-1} temporal frequency and 0.3 cycles deg^{-1} spatial frequency) or a wide dark bar (38 deg s^{-1} speed, 6.5 deg width) in four orientations, drifting in eight different directions (separated by 45 deg) repeated twice for each orientation. Full field ON-OFF flashes were presented in blocks of 10 repetitions of 0.5 s OFF, 1 s ON and 0.5 s OFF stimuli.

Data analysis

Preprocessing. Initial analysis was performed in MATLAB R2018b and later in MATLAB R2019a. Raw voltage traces were high-pass filtered (300 Hz) and spikes were detected and sorted using Kilosort2 (https://github.com/cortex-lab/Kilosort) and Phy as previously described[45], followed by manual curation. Firing rates histograms were calculated as the average firing rate across 16.7 ms time bins. Analog input channels (Photodiode, camera trigger) were extracted in MATLAB (MathWorks, Inc.) and arduino were recorded at a 20 kHz sample rate and were used for offline synchronisation. Custom-made scripts in MATLAB were used to extract the time points of the visual stimulus onsets and matched to the corresponding video camera frame.

Determining the surface of the superficial superior colliculus (sSC). Initial SC location was determined in real-time by auditory monitoring of multi-unit activity to a flashing stimulus and was later confirmed offline using a current source density analysis of the raw recording (see[46,47]) combined with histological reconstruction of the probe location visualised with DiI. CSD profiles were calculated for each recording and were used to align the depth of the units across recordings and across animals. The transition point between an overlying source and underlying sink was taken as the boundary between the stratum griseum superficiale (SGS) and the stratum opticum (SO). The boundary between the superficial (sSC) and intermediate/deep superior colliculus (idSC) was defined as 100 µm below this inflection depth (ID), taking into account the thickness of the SO. sSC was defined as 300 µm above the ID to 100 µm below the ID, and idSC was defined as the area below 100 µm below the ID. Only units identified as within the sSC and units with at least 2 spikes within the stimulus presentation were used for analysis. For all analyses spikes were sorted into peristimulus periods based on synchronisation with the stimulus frames and firing-rate histograms were calculated over 16.7 ms time bins.

Analysis of baseline firing properties. Responses to a full field grey screen during the first 60s of recording were taken to determine the baseline firing properties of the recorded cells. The baseline firing rate per animal was calculated as the mean firing rate across cells in the 1000 μm below the sSC surface.

Analysis of responses to flash stimulus. Responses to a single flash stimulus (0.5 s OFF; 1 s ON; 0.5 s OFF) were generated by averaging the firing-rate histograms across 10 repetitions of the stimulus. The responsiveness of single units was defined based on the p-value generated from running a ZETA test[48] on the average firing rate histograms using the 30 s period before the stimulus as baseline and the 2 s flash stimulus as the response time. Clustering of responsive units was done using K-means and the number of clusters was determined by identifying the elbow point when analysing the Calinski-Harabasz index. Clustering was done with units from both genotypes pooled together, then later split based on genotype. The proportion of flash responsive cells for *Ptchd1* and *Cul3* animals were determined for each animal by dividing the number of sSC units that were $p < 0.05$ by the total number of sSC units found.

Analysis of responses to loom stimulus. Responses to a single loom stimulus were obtained by averaging the responses to the first loom of the loom bout stimulus (consisting of 5 consecutive looms) across 10 repetitions. Responsiveness was again defined as units having a *p*-value (determined using the ZETA test) of < 0.05, with the 30 s preceding the loom stimulus as baseline and the 0.7 s of first loom presentation as the response time. The average firing rate was calculated as the overall average of the mean firing-rate recorded across each of the 5 loom presentations individually for 10 repetitions. Maximum firing was similarly calculated as the mean maximum firing during each of the 5 looms, averaged across 10 repetitions. The time-to-peak was calculated as the mean of the time to the peak firing within each of the 5 looms, averaged over the 10 repetitions.

Analysis of responses to shifting white noise stimulus. To further analyse the visual receptive fields (RFs) of the units recorded we analysed their responses to a shifting white noise stimulus[44] and calculated them as spike-triggered averages. The location of the centre of the receptive field was estimated by finding the pixel with the highest variance over a peri-spike time period and the final RF was cropped to 160 x 160 pixels centred on this pixel of highest variance. To find the signal-to-noise ratio (SNR) for each neuron, we first found the difference between the square of the pixel value at the receptive field centre and the variance of all the values in a 5 pixels border around the edge of the RF. The $\log_{10}$ of this value was then multiplied by 10 to obtain the SNR value. Visually-responsive neurons were defined as those with SNRs in the 80th percentile of the SNRs of all sSC units or above. The centre of the RF was assigned as ON or OFF based on the sign of the mean of the central pixel at the centre of the receptive field. The proportion of OFF RFs was calculated as the ratio between visually-responsive cells with OFF RFs and the total number of visually-responsive cells in the sSC. The radius of the RF centre was calculated as the width at half-peak of the spatial RF profile. The average radius of the receptive fields of an animal was calculated using only the visually-responsive units. Temporal receptive fields were clustered similarly to flash responses, using K-means to cluster the responses and the number of clusters determined using the Calinski-Harabasz index.

Analysis of responses to moving bars and gratings stimuli. For each direction the mean across trials was calculated and normalised to the baseline firing in the 30 s before stimulus onset. The preferred direction (D_p) was defined as the direction with the greatest normalised response and the non-preferred direction (D_{np}) was taken as 180 degrees from that angle. The direction selectivity index (DSI) was then computed as $(D_p-D_{np})/(D_p+D_{np})$ with values falling in a range from 1 (high direction selectivity) to 0 (low direction selectivity). Units were defined as being 'direction selective' (DS) if their DSI was in the 80th percentile or higher out of all units recorded within the sSC. The proportion of direction selective cells per animal was found by quantifying the proportion of DS sSC units divided by all sSC units recorded for that animal.

Head-fixed behavioural analysis

The motion of the animal was determined by sorting the difference between pixels in neighbouring frames with K-means into two groups. The proportion of time each animal spent running was calculated as the proportion of frames that were registered as 'moving' over the total number of frames. The pupillary light reflex (PLR) of the animals was assessed by tracking the change in pupil size across the repetitions of the flash stimulus. A deep neural network approach for markerless tracking[49] was used to extract points around the pupil. The diameter of the pupil was then calculated by fitting an ellipse to these points. Since we observed, and it is known, that the size of the pupil is greatly affected by locomotion, when analysing the PLR we only included repetitions in which the mice were running. An animal was considered to be running during a repetition if the mouse was classified as 'moving' in over half of the video frames covering that repetition.

In vitro **electrophysiology**

Mice were deeply anesthetised via intraperitoneal (i.p.) injection of ketamine (95 mg kg^{-1}) and xylazine (4.5 mg kg^{-1}), followed by transcardial perfusion with ice-cold, oxygenated (95 % O_2, 5 % CO_2) artificial cerebrospinal fluid (ACSF) containing (in mM): 118 NaCl, 2.5 KCl, 1.25 NaH_2PO_4, 1.5 $MgSO_4$, 1 $CaCl_2$, 10 Glucose, 3 Myo-inositol, 30 Sucrose, 30 $NaHCO_3$; pH = 7.4. The brain was rapidly excised and coronal sections of 300 µm thickness containing the SC and PAG were cut using a Linear-Pro7 vibratome (Dosaka, Japan). Slices were left to recover for 20 min at 35°C, followed by a slow cool down to room temperature (RT) over 40 – 60 min. After recovery, one slice was transferred to the recording chamber (RC-26GLP, Warner Instruments, Holliston, MA, USA) and superfused with ACSF containing 2 mM $CaCl_2$ and 20 µM bicuculline methiodide (Tocris) at a rate of 3 – 4 ml/min at RT. In experiments using 100 nM α-dendrotoxin (Alomone Labs, Jerusalem, Israel), 0.1 % bovine serum albumin (BSA) was added to the ACSF. Glass pipettes (B150-86-10, Sutter Instrument, Novato, CA, USA) with resistances of 3 – 4 MΩ were crafted using a P1000 horizontal pipette puller (Sutter Instrument) and filled with internal solution containing (in mM): 130 K-Gluconate, 10 KCl, 5 $MgCl_2$, 5 MgATP, 0.2 NaGTP, 0.5 EGTA, 5 HEPES; pH 7.4 adjusted with KOH. Biocytin (0.2 – 0.3 %) was added to the internal solution for post hoc morphological reconstruction. Neurons of the dPAG or the dmSC were visually identified using an infrared differential interference contrast video system in a BX51 microscope (Olympus, Tokyo, Japan). Electrical signals were acquired at 20 – 50 kHz and filtered at 4 kHz using a Multiclamp 700B amplifier (Molecular Devices, San Jose, CA, USA) connected to a Digidata 1440A digitizer (Molecular Devices) with pClamp10 software (Molecular Devices). Spontaneous excitatory postsynaptic currents (sEPSCs) were recorded at –60 mV for at least 1 min. Intrinsic membrane properties and neuronal excitability were measured in current clamp mode by applying current steps from –20 to 200 pA for 1 s in 10 pA increments. Access resistance was constantly monitored between protocols and recordings with access resistances exceeding 20 MΩ or with changes in access resistance or holding current by more than 20 % were discarded. After recordings, the pipette was carefully withdrawn and the slice was transferred to 4 % paraformaldehyde (PFA) in PBS solution.

Analysis: Whole-cell recordings were analysed in Clampfit (Molecular Devices) and MiniAnalysis Program (Synaptosoft). Resting membrane potential (RMP) was measured as the average membrane potential prior to current-injection. Input resistance (R_{in}) was calculated from the slope of the linear fit of the hyperpolarising current/voltage relationship. Membrane time constant τ was measured from the exponential fit of the membrane potential change in response to a –10 or –20 pA current-injection. Membrane capacitance (C_m) was calculated from $C_m = \tau/R_{in}$. Action potential firing was quantified in Clampfit using the event detection function. Phase-plane plots were performed to investigate the dynamic changes in the membrane potential over time (dV/dt) and were generated using the spikes from the first current step necessary to elicit action potentials (rheobase current). Soma size was calculated by fitting an oval to the projected image (63X) of the neurons and calculating the area of that oval.

Histology

For fluorescent immunostainings and histological confirmation of fibre and probe locations, adult *Setd5*$^{+/+}$ and *Setd5*$^{+/-}$ mice were transcardially perfused with 4 % paraformaldehyde (PFA) and their brains were dissected, post-fixed overnight in 4 % PFA, washed with 1X PBS, dehydrated in a 30 % sucrose solution and sectioned with a freezing microtome (SM2010R, Leica) to 100 µm (for probe/fibre confirmation) and 40 µm (for immunostainings) thick slices. For histological confirmation of probe and fibre locations, the sections were rinsed in PBS, stained with 4',6-diamidino-2-phenylindole (DAPI; 2 mM in PBS) and mounted on Superfrost glass slides in a mounting medium containing 1,4-diazabicyclooctane (DABCO; Sigma, D27802) and Mowiol 4-88 (Sigma, 81381). For Kv1.1 immunostainings, tissue was rinsed and then blocked for 1 hour at room temperature in a buffer solution containing 10% normal donkey serum (Abcam, ab7475), 0.1 % Triton X-100 in PBS. Primary antibodies (Kv1.1, Rabbit, 1:200; Rb-Af400, Frontier Institute) were diluted in a blocking buffer and incubated for 48 hours at 4 ºC. The tissue was then rinsed 3 times in PBS and left overnight to wash at 4 ºC. Secondary antibodies (Alexa-594 Donkey anti-rabbit, 1:1000; R37119, Thermo Fisher) were diluted in 1X PBS and incubated for 2 hrs at room temperature in the dark, before being washed three more times in 1X PBS before being counter-stained with DAPI and mounted as for histological sections described above. Sections were imaged with either a confocal microscope (LSM800, Zeiss), at 63X or 20X magnification, or a wide-field microscope (VS120, Olympus), at 10X magnification. For comparison between the Kv1.1 expression in *Setd5*$^{+/+}$ and *Setd5*$^{+/-}$ tissue 30 µm stacks were imaged with 1 µm sections at 63X magnification, or 55 µm stacks were imaged with 2 µm sections at 20X magnification, and the same laser power settings were used for all images at a given magnification.

For visualisation of the dPAG/dmSC cells recorded *in vitro* tissue sections were washed in 1X PBS for 10 minutes then a solution of Streptavidin (1:100, 1mg/ml, Thermo Fisher Scientific, S11227) in PBS with 0.3% Triton-X was added and the samples were left at 4 ºC overnight. The tissue was then washed three times with PBS, mounted into a custom designed chamber for thick slices and imaged with a confocal microscope (LSM800, Zeiss) at 20X (90 µm projection, 2 µm sections) and 40X (50 µm projection, 1 µm sections).

Western blot

Tissue samples from the superior colliculus, periaqueductal grey (PAG) and cortex were dissected from *Setd5*$^{+/+}$ (n = 3) and *Setd5*$^{+/-}$ (n = 3) mice. PAG tissue was dissected using a 2 mm diameter biopsy punch (ID: 2 mm, OD: 3 mm, Fine Science Tools, 18035-02). Each purification was performed independently three times and samples were stored at -80 ºC until further processing. Samples were Dounce homogenized 15 times with 300 mL RIPA buffer (50 mM Tris-HCl, 150 mM NaCl, 0.5 % sodium deoxycholate, 1 % Triton-X, 0.2 % SDS, completeTM protease inhibitor cocktail (Roche) and and 1 mM phenylmethylsulfonyl fluoride (PMSF, Sigma)) using the loose pestle and sonicated for 10 seconds. The lysed samples were centrifuged for 20 min at 16000 *g* and the supernatant was stored at -80ºC. Total protein concentration was determined using the BCA protein assay (Pierce). Proteins were boiled for 5 min in Laemmli sample buffer before being separated at 200V for 40 min using TGX stain-free precast gels (Bio-Rad). Stain-free protein gels were activated with UV light for 5 min and then transferred to PVDF membranes (Bio-Rad) using a turbo transfer system (Bio-Rad). Membranes were blocked for 1 hr in TBST (Tris-buffered saline with 0.1 % Tween 20) supplemented with 5 % bovine serum albumin (Sigma) and then incubated overnight at 4 ºC with anti-Kv1.1 primary antibody (Rb-Af400, Frontier Institute, 1:100). After primary antibody incubation, membranes were washed four times with TBST for 5 min and then incubated with anti-rabbit IRDye 800CW (LI-COR Biosciences, dilution 1:4000) for 1 hr at room temperature. Bio-Rad ChemiDoc MP system was used for imaging and acquisition.

Statistics

Analyses were performed in custom-written MATLAB (2019a) scripts (MathWorks, Inc.). Shapiro-Wilk and Levene's tests were used to test the normality and the equal variances of the datasets, respectively and were parametric or non-parametric tests used accordingly. All statistical tests are reported in the text and appropriate figure legends ($^{*}p < 0.05$, $^{**}p < 0.01$, $^{***}p < 0.001$). In bar plots the mean ± s.e.m. are shown, unless otherwise stated. Boxplots display the median and IQR. Please see the Supplementary Table 1 for detailed statistical analysis.

Supplementary Material

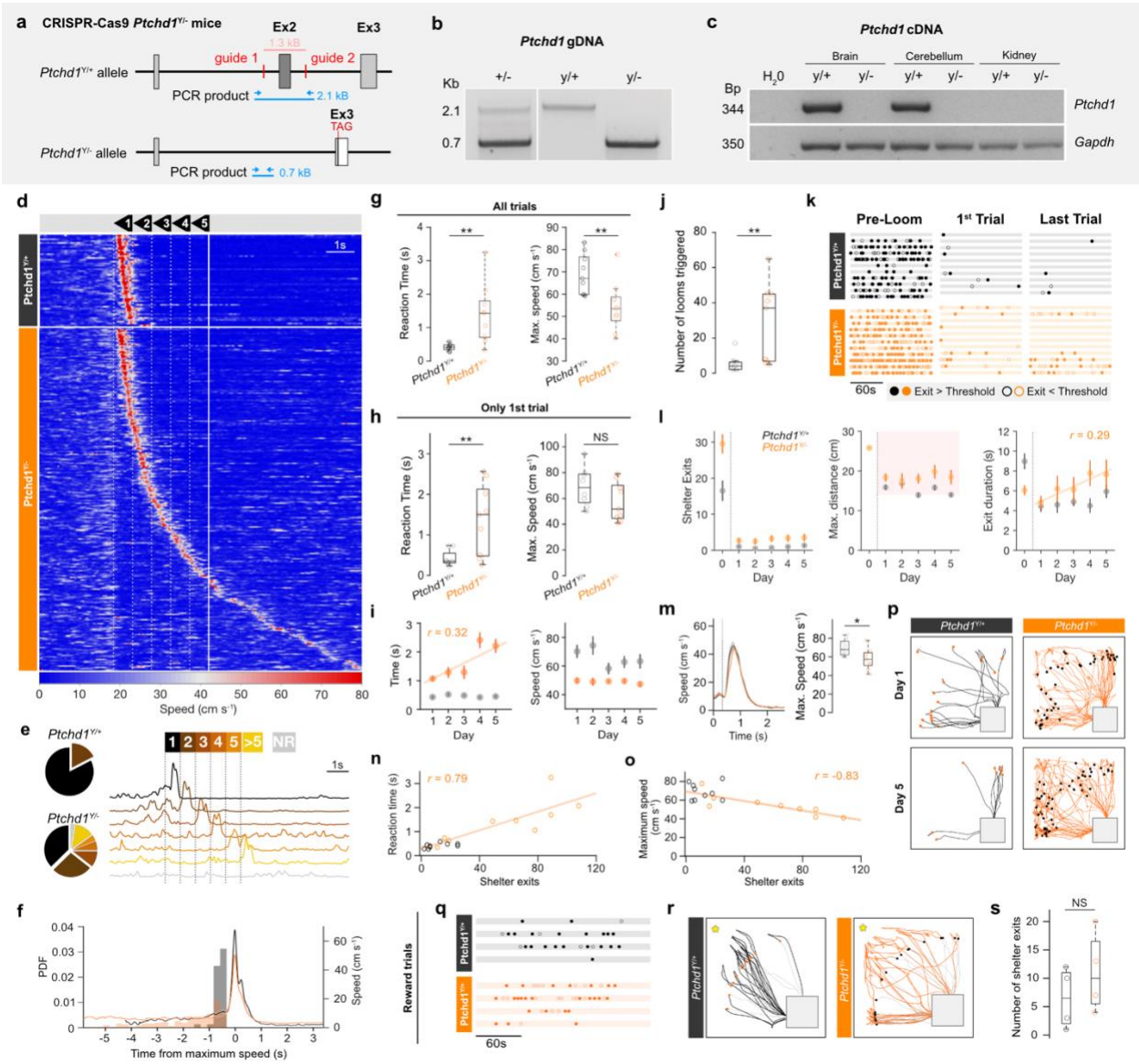

Supplementary Figure 1. *Ptchd1* - new knockout mouse model and behavioural analysis to the LAR. a, CRISPR-Cas9 design for the generation of *Ptchd1*$^{Y/-}$ mice. **b**, gDNA confirmation of the excised DNA (2.1 Kb in *Ptchd1*$^{Y/+}$ and 0.7 Kb in *Ptchd1*$^{Y/-}$). **c**, Confirmation of loss of Ptchd1 cDNA in different tissues in *Ptchd1*$^{Y/-}$ mice, and control *Gapdh* presence throughout. **d**, Raster plot of mouse speed in response to looming stimuli (white, dotted vertical lines denote the start of each loom; white solid line denotes the end of the stimulus) for *Ptchd1*$^{Y/+}$ (top, 49 trials) and *Ptchd1*$^{Y/-}$ (bottom, 259 trials), sorted by reaction time. **e**, Proportion of trials where the mice respond within 1 of the 5-loom stimuli, after the 5th or not at all (left, *Ptchd1*$^{Y/+}$, top and *Ptchd1*$^{Y/-}$, bottom; Proportion of trials where mice escaped within the first loom: *Ptchd1*$^{Y/+}$, 0.826, *Ptchd1*$^{Y/-}$, 0.374, $P = 0.004$). Distribution of the number of looms to escape, *Ptchd1*$^{Y/+}$, *Ptchd1*$^{Y/-}$, $p < 0.001$) and example traces from each category (right). **f**, Kinetics of the escape response to the looming stimulus and histograms of time stimulus start with respect to the peak of the escape (*Ptchd1*$^{Y/+}$, black; *Ptchd1*$^{Y/-}$, orange, $p < 0.001$). **g**, Mean reaction time (left) and maximum escape speed (right) per animal, for all trials where the mouse responded (Reaction time; *Ptchd1*$^{Y/+}$, 0.411s, *Ptchd1*$^{Y/-}$, 1.41 s, P = 0.002. Maximum escape speed; *Ptchd1*$^{Y/+}$, 69.1 cms^{-1}, *Ptchd1*$^{Y/-}$, 54.2 cms^{-1}, $P = 0.005$). **h**, Mean reaction time (left) and maximum escape speed (right) per animal, for the very first loom presentation. (Reaction time; *Ptchd1*$^{Y/+}$, 0.423 s,

Ptchd1$^{Y/-}$, 1.39 s, $P = 0.014$. Maximum escape speed; *Ptchd1*$^{Y/+}$, 69.1 cms^{-1}, *Ptchd1*$^{Y/-}$, 57.3 cms^{-1}, $P = 0.139$) **i**, Relationship between reaction time and test day (*Ptchd1*$^{Y/+}$, $r = 0.029$, $P = 0.840$; *Ptchd1*$^{Y/-}$, $r = 0.317$, $P < 0.001$, Pearson's *r*, left) and maximum escape speed and test day (*Ptchd1*$^{Y/+}$, $r = -0.254$, $P = 0.07$; *Ptchd1*$^{Y/-}$, $r = -0.040$, $P = 0.556$, Pearson's *r*, right). **j**, Average total number of looms triggered per animal across the 5 days of standard LAR testing (*Ptchd1*$^{Y/+}$, 5.44 looms; *Ptchd1*$^{Y/-}$, 28.8 looms, $P = 0.0043$). **k**, Ethogram of shelter exits during the pre-stimulus exploration period (left), during the first trial (centre) and during the last trial on day 5 (right). Filled and open dots represent exits into the threat zone or not, respectively. **l**, Relationship between test day and the number of exits from (left, *Ptchd1*$^{Y/+}$, $r = 0.122$, $P = 0.134$; *Ptchd1*$^{Y/+}$, $r = 0.101$, $P = 0.1936$, Pearson's *r*), the maximum distance travelled from (centre, *Ptchd1*$^{Y/+}$, $r = -0.213$, $P = 0.071$; *Ptchd1*$^{Y/+}$, 112 trials, $r = 0.103$, $P = 0.278$, Pearson's *r*) and the duration of time spent outside of the shelter (right, *Ptchd1*$^{Y/+}$, $r = 0.148$, P = 0.214; *Ptchd1*$^{Y/+}$, $r = 0.286$, $P = 0.002$, Pearson's *r*)**. m**, Mean response kinetics of *Ptchd1*$^{Y/+}$ (black) and *Ptchd1*$^{Y/-}$ (orange) of trials where the mice respond within the first loom presentation (L1 trials). Shaded area: s.e.m., left. Average maximum speed reached during L1 trials (*Ptchd1*$^{Y/+}$, 69.8cms^{-1}; *Ptchd1*$^{Y/-}$, 57.6 cms^{-1}; $P = 0.024$). **n**, Relationship between the average reaction time and the total number of shelter exits per animal (*Ptchd1*$^{Y/+}$, n = 9, $r = 0.549$, $P = 0.126$; *Ptchd1*$^{Y/-}$, n = 9, $r = 0.789$, $P = 0.012$, Pearson's *r*). **o**, Relationship between the average maximum escape speed and the total number of shelter exits per animal (*Ptchd1*$^{Y/+}$, n = 9, $r = 0.018$, $P = 0.963$; *Ptchd1*$^{Y/-}$, n = 9, $r = -0.829$, $P = 0.0057$, Pearson's *r*). **p**, Trajectories of the escape paths during LAR trials on the first test day (top) and the last test day (bottom) for *Ptchd1*$^{Y/+}$ (black) and *Ptchd1*$^{Y/-}$ (orange). Filled dots indicate the position of the mouse at the start of the stimulus. **q**, Ethogram as in **k** but during the reward trials. Each row corresponds to the trial of an individual animal. **r**, Outward trajectories before stimulus (light grey) and inbound trajectories after the onset of the stimulus for *Ptchd1*$^{Y/+}$ (black) and *Ptchd1*$^{Y/-}$ (orange) during the reward trials. **s**, Total number of shelter exits during the reward trial (*Ptchd1*$^{Y/+}$, n = 4, 6.5 exits; *Ptchd1*$^{Y/-}$, n = 4, 11 exits, $P = 0.343$). Box-and-whisker plots show median, IQR and range. Shaded areas show s.e.m.. *P*-values: Wilcoxon's test, *p*-values: two-sample KS test, unless otherwise stated. For detailed statistics, see Supplementary Table 1.

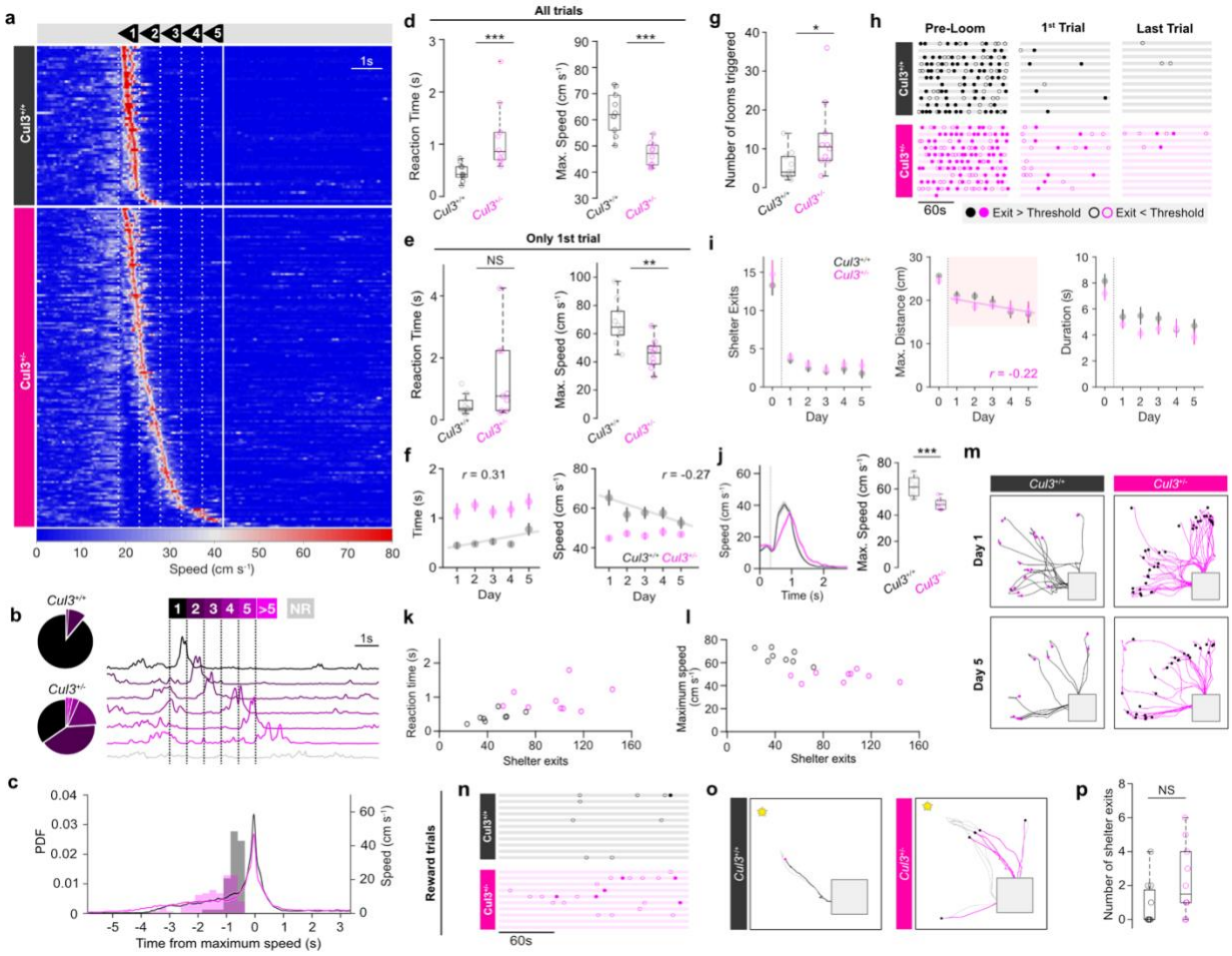

Supplementary Figure 2. Behavioural analysis of *Cul3* mice to the LAR. a, Raster plot of mouse speed in response to the looming stimuli (white, dotted vertical lines denote the start of each loom; white solid line denotes the end of the stimulus) for *Cul3*$^{+/+}$ top, 61 trials) and *Cul3*$^{+/-}$ (bottom, 112 trials), sorted by reaction time. **b**, Proportion of trials where the mice respond within 1 of the 5-loom stimuli, after the 5th or not at all (left, *Cul3*$^{+/+}$, top and *Cul3*$^{+/-}$, bottom; Proportion of trials where mice escaped within the first loom: *Cul3*$^{+/+}$, 0.892, *Cul3*$^{+/-}$, 0.347, $P < 0.001$) and example traces from each category (right). **c**, Kinetics of the escape response to the looming stimulus in *Cul3*$^{+/+}$ and *Cul3*$^{+/-}$ animals. Histogram of time between the stimulus start and the maximum escape speed and the mean response kinetics of *Cul3*$^{+/+}$ (black) and *Cul3*$^{+/-}$ orange) aligned by their time of maximum speed. **d**, Mean reaction time (left) and maximum escape speed (right) per animal, for all trials where the mice responded. (Reaction time; *Cul3*$^{+/+}$, 0.464 s, *Cul3*$^{+/-}$, 1.11 s, $P < 0.001$. Maximum escape speed; *Cul3*$^{+/+}$, 62.7 cms^{-1}, *Cul3*$^{+/-}$, 46.8 cms^{-1}, $P < 0.001$). **e**, Mean reaction time (left) and maximum escape speed (right) per animal, for the very first loom presentation. (Reaction time; *Cul3*$^{+/+}$, 0.446 s, *Cul3*$^{+/-}$, 1.26 s, $P = 0.117$. Maximum escape speed; *Cul3*$^{+/+}$, 67.5 cms^{-1}, *Cul3*$^{+/-}$, 45.8 cms^{-1}, $P = 0.003$). **f**, Correlation between reaction time and test day (*Cul3*$^{+/+}$, $r = 0.3146$, $P = 0.012$; *Cul3*$^{+/-}$, $r = 0.109$, $P = 0.233$, Pearson's r, left) and maximum escape speed and test day (*Cul3*$^{+/+}$, $r = -0.2679$, $P = 0.033$; *Cul3*$^{+/-}$, $r = 0.125$, $P = 0.1711$, Pearson's r, right). **g**, Average total number of looms triggered per animal across the 5 days of testing (*Cul3*$^{+/+}$, 5.6 looms, *Cul3*$^{+/-}$, 12.9 looms, $P = 0.023$). **h**, Ethogram of shelter exits during the pre-stimulus exploration period (left), during the first trial (centre) and during the last trial on day 5 (right). Filled and open dots represent exits into the threat zone or not, respectively. **i**, Relationship between test day and the number of exits from (left, *Cul3*$^{+/+}$, $r = 0.083$, $P = 0.289$; *Cul3*$^{+/-}$, $r = -0.1198$, $P = 0.1253$, Pearson's r), the maximum distance travelled (centre, *Cul3*$^{+/+}$, $r = -0.081$, $P = 0.480$; *Cul3*$^{+/-}$, $r = -0.224$, $P = 0.034$, Pearson's r) and the duration of time spent outside of the shelter (right, *Cul3*$^{+/+}$, $r = -0.036$, $P = 0.754$; *Cul3*$^{+/-}$, $r = -0.091$, $P = 0.393$). **j**, Mean response kinetics

of *Cul3*$^{+/+}$ (black) and *Cul3*$^{+/-}$ (orange) of trials where the mice respond within the first loom presentation (L1 trials). Shaded area: s.e.m., left. Average maximum speed reached during L1 trials (*Cul3*$^{+/+}$, 55 trials, 59.6 cms^{-1}; *Cul3*$^{+/-}$, 41 trials, 45.8 cms^{-1}; $P < 0.001$). **k**, Relationship between the average reaction time and the total number of shelter exits per animal (*Cul3*$^{+/+}$, n = 10, $r = 0.656$, $P = 0.078$; *Cul3*$^{+/-}$, n = 10, $r = 0.219$, $P = 0.571$, Pearson's r). **l**, Relationship between the average maximum escape speed and the total number of shelter exits per animal (*Cul3*$^{+/+}$, n = 10, $r = -0.671$, $P = 0.069$; *Cul3*$^{+/-}$, n = 10, $r = -0.011$, $P = 0.977$, Pearson's r). **m**, Trajectories of the escape paths during LAR trials on the first test day (top) and the last test day (bottom) for *Cul3*$^{+/+}$ (black) and *Cul3*$^{+/-}$ (magenta). Filled dots indicate the position of the mouse at the start of the stimulus. **n**, Ethogram as in **h** but during the reward trials, left. Each row corresponds to the trial of an individual animal. **o**, Outward trajectories before stimulus (light grey) and inbound trajectories after the onset of the stimulus (*Cul3*$^{+/+}$ (black) and *Cul3*$^{+/-}$ (orange)) during the reward trial. **p,** Total number of shelter exits during the reward trial, right (*Cul3*$^{+/+}$, n = 10, 0.9 exits, *Cul3*$^{+/-}$, n = 10, 2.1 exits, P = 0.150). Box-and-whisker plots show median, IQR and range. Shaded areas show s.e.m.. P-values: Wilcoxon's test, p-values: two-sample KS test, unless otherwise stated. For detailed statistics, see Supplementary Table 1.

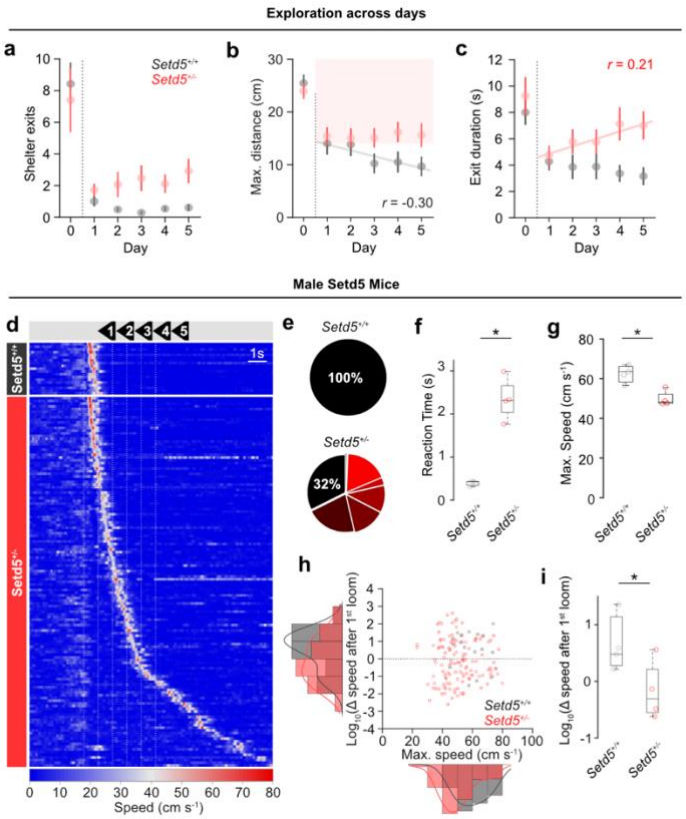

Supplementary Figure 3. Behavioural analysis of LAR in male *Setd5* mice. a-c, Adaptation in exploration, average maximum distance and shelter exit duration across days. Shaded area represents the threat zone (**a**, Setd5$^{+/+}$: p = 0.2189, *Setd5*$^{+/-}$: p = 0.4974; **b**, *Setd5*$^{+/+}$: p = 0.0366, *Setd5*$^{+/-}$: p = 0.7918; **c,** *Setd5*$^{+/+}$: p = 0.4974, *Setd5*$^{+/-}$: p = 0.0191). **d**, Raster plot of mouse speed in response to the looming stimuli (white, dotted vertical lines denote the start of each loom; white solid line denotes the end of the stimulus) for Setd5$^{+/+}$ (top, n = 4, 18 trials) and *Setd5*$^{+/-}$ (bottom, n = 4, 144 trials), sorted by reaction time. **e**, Summary of the proportion of trials in which the mice respond *within each loom* for *Setd5*$^{+/+}$ (top) and *Setd5*$^{+/-}$ mice (bottom). Proportion of trials where mice escaped within the first loom: Setd5$^{+/+}$, 1.00, *Setd5*$^{+/-}$, 0.324, P = 0.028. Distribution of number of looms to escape, *Setd5*$^{+/+}$, 18 trials, *Setd5*$^{+/-}$, 144 trials, p < 0.001. **f**, Summary of the average reaction time per animal (Setd5$^{+/+}$, 18 trials, 0.394 s; *Setd5*$^{+/-}$, 130 trials, 2.10 s, P = 0.029). **g**, Summary of the average maximum escape speed per animal (Setd5$^{+/+}$, n = 18, 63.3 cms^{-1}; *Setd5*$^{+/-}$, n = 130, 49.9 cms^{-1}, P = 0.047). **h**, Scatter-hist plot of the $\log_{10}$(change in speed upon the 1st loom presentation) (x-axis, see methods) and the maximum speed reached during the escape (y-axis), (Log_{10}(**Δ**Speed): *Setd5*$^{+/+}$, 18 trials, 0.622, *Setd5*$^{+/-}$, 144 trials, -0.128, p = 0.008; Maximum Escape Speed; *Setd5*$^{+/+}$, 18 trials, 59.7 cms^{-1}, *Setd5*$^{+/-}$, 144 trials, 49.6 cms^{-1}, p = 0.005). **i**, Summary of the average Log_{10}(**Δ**Speed) per animal for Setd5$^{+/+}$ (0.684) and Setd5$^{+/-}$ (-0.169, P = 0.048). Box-and-whisker plots show median, IQR and range. Shaded areas show s.e.m.. P-values: Wilcoxon's test, p-values: two-sample KS test. For detailed statistics, see Supplementary Table 1.

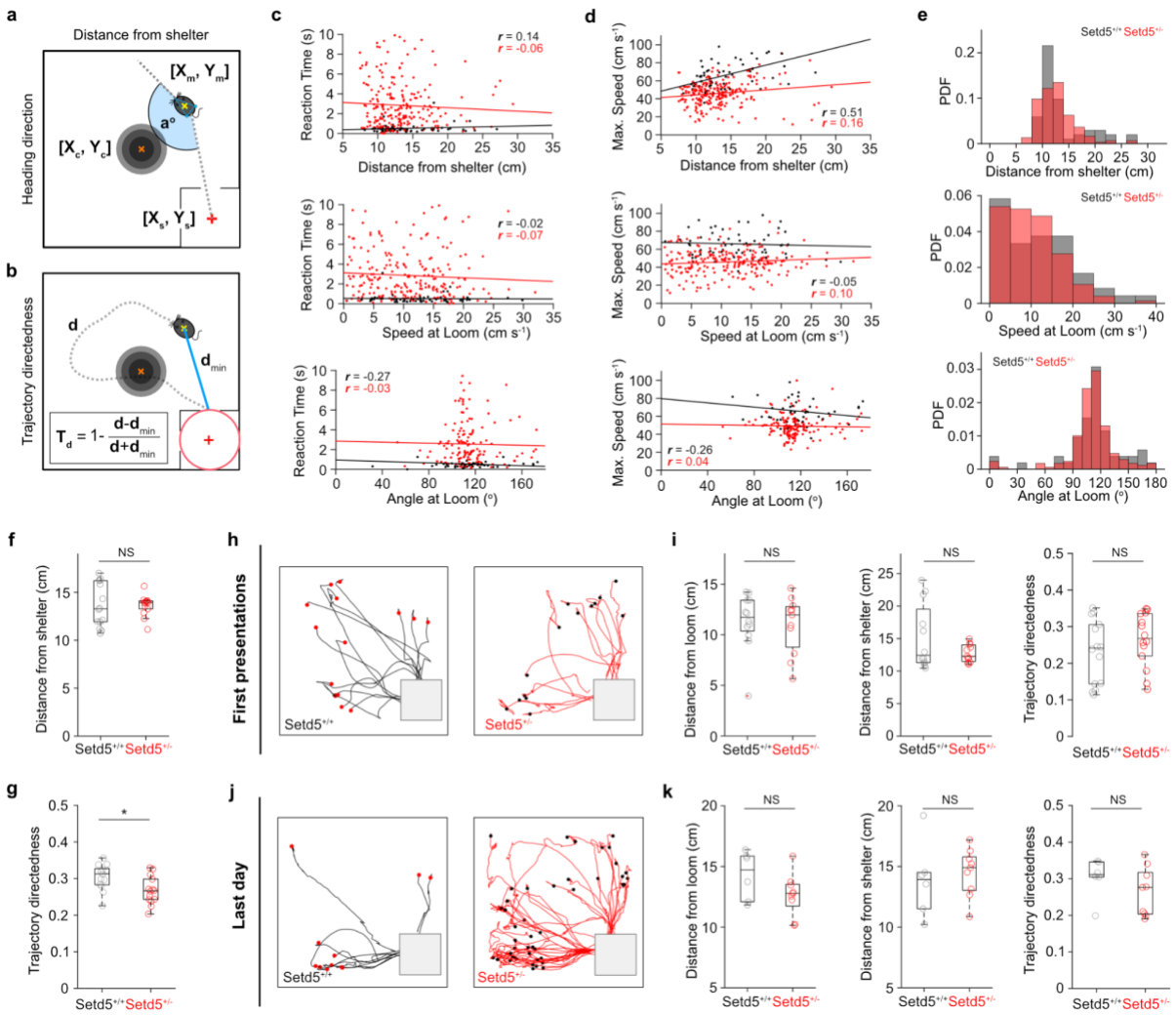

Supplementary Figure 4. Position and head direction do not account for deficits in LAR. a, Schematic describing how the distance from the shelter (difference between centre of the mouse ([X_m, Y_m], yellow cross, and the centre of the shelter ([X_s, Y_s], red cross), distance from the loom (difference between centre of the mouse ([X_m, Y_m], yellow cross, and the centre of the arena ([X_c, Y_c], orange cross) and the heading direction (Angle ABC where A is the tip of the mouse's nose (blue dot), B is the centre position between the back two paws (blue dot) and C is the centre of the shelter ([X_s, Y_s], red cross); 0° would be facing the centre of the shelter) are calculated. **b**, Schematic describing how trajectory directedness (T_d) is calculated. See methods for more details. **c**, Relationship between reaction time and the distance of the mouse from the shelter when the stimulus started (top, *Setd5*$^{+/+}$, $r(59) = 0.144$, P = 0.267; *Setd5*$^{+/-}$, $r(196) = -0.058$, P = 0.391, Pearson's *r*), the speed of the mouse at the start of the stimulus (middle, *Setd5*$^{+/+}$, $r(59) = -0.0242$, P = 0.853; *Setd5*$^{+/-}$, $r(196) = -0.069$, P = 0.304, Pearson's *r*) and the heading angle of the mouse at the start of the stimulus (bottom, *Setd5*$^{+/+}$, $r(59) = -0.2735$, P = 0.049; *Setd5*$^{+/-}$, $r(196) = -0.032$, P = 0.693, Pearson's *r*). **c**, Relationship between maximum escape speed and the distance of the mouse from the shelter when the stimulus started (top, *Setd5*$^{+/+}$, $r(59) = 0.510$, P < 0.001; *Setd5*$^{+/-}$, $r(196) = 0.161$, P = 0.015, Pearson's *r*), the speed of the mouse at the start of the stimulus (middle, *Setd5*$^{+/+}$, $r(59) = -0.052$, P = 0.688; *Setd5*$^{+/-}$, $r(196) = 0.099$, P = 0.137, Pearson's *r*) and the heading angle of the mouse at the start of the stimulus (bottom, *Setd5*$^{+/+}$, $r(59) = -0.259$, P = 0.062; *Setd5*$^{+/-}$, $r(196) = 0.042$, P = 0.611, Pearson's *r*). **e**, Probability density functions of the distance from the shelter (top, *Setd5*$^{+/+}$, black, 60 trials; *Setd5*$^{+/+}$, red, 198 trials, p = 0.421), the mouse's speed at the start of the stimulus (middle, *Setd5*$^{+/+}$,

black, 60 trials; *Setd5*$^{+/+}$, red, 198 trials, p = 0.164) and the heading angle at the start of the stimulus (bottom, *Setd5*$^{+/+}$, black, 60 trials; *Setd5*$^{+/+}$, red, 198 trials, p = 0.606). **f**, Summary of the average distance from the shelter (*Setd5*$^{+/+}$, n = 14, 13.7 cm; *Setd5*$^{+/-}$, n = 14, 13.6 cm, P = 0.696, two-tailed *t*-test). **g**, Summary of the average trajectory directedness (*Setd5*$^{+/+}$, n = 14, 0.304; *Setd5*$^{+/-}$, n = 14, 0.267, P = 0.014, two-tailed *t*-test). **h**, Escape path trajectories of *Setd5*$^{+/+}$ (14 trials, black, left) and *Setd5*$^{+/-}$ (14 trials, red, left) to their first loom presentation. Filled dots represent the position of the mouse at the start of the stimulus. **i**, Summary of the average distance from the loom (left, *Setd5*$^{+/+}$, 14 trials, 11.3 cm; *Setd5*$^{+/+}$, 14 trials, 11.0 cm, P = 0.892), average distance from the shelter (centre, *Setd5*$^{+/+}$, 14 trials, 15.2 cm; *Setd5*$^{+/+}$, 14 trials, 12.7 cm, P = 0.689) and trajectory directedness (right, *Setd5*$^{+/+}$, 14 trials, 0.230; *Setd5*$^{+/+}$, 14 trials, 0.2637, P = 0.223) during the first loom presentations. **j**, As for **h** but for trials from the last day of testing. *Setd5*$^{+/+}$ (9 trials, black, left) and *Setd5*$^{+/-}$ (43 trials, red, left). **k**, Summary of the average distance from the loom (left, *Setd5*$^{+/+}$, 14 trials, 14.3 cm; *Setd5*$^{+/+}$, 14 trials, 12.7 cm, P = 0.223), average distance from the shelter (centre, *Setd5*$^{+/+}$, 14 trials, 13.9 cm; *Setd5*$^{+/+}$, 14 trials, 14.5 cm, P = 0.388) and trajectory directedness (right, *Setd5*$^{+/+}$, 14 trials, 0.303; *Setd5*$^{+/+}$, 14 trials, 0.264, P = 0.328) during the trials on the last test day. Box-and-whisker plots show median, IQR and range. Shaded areas show s.e.m.. P-values: Wilcoxon's test, p-values: two-sample KS test, unless otherwise stated. For detailed statistics, see supplementary Table 1.

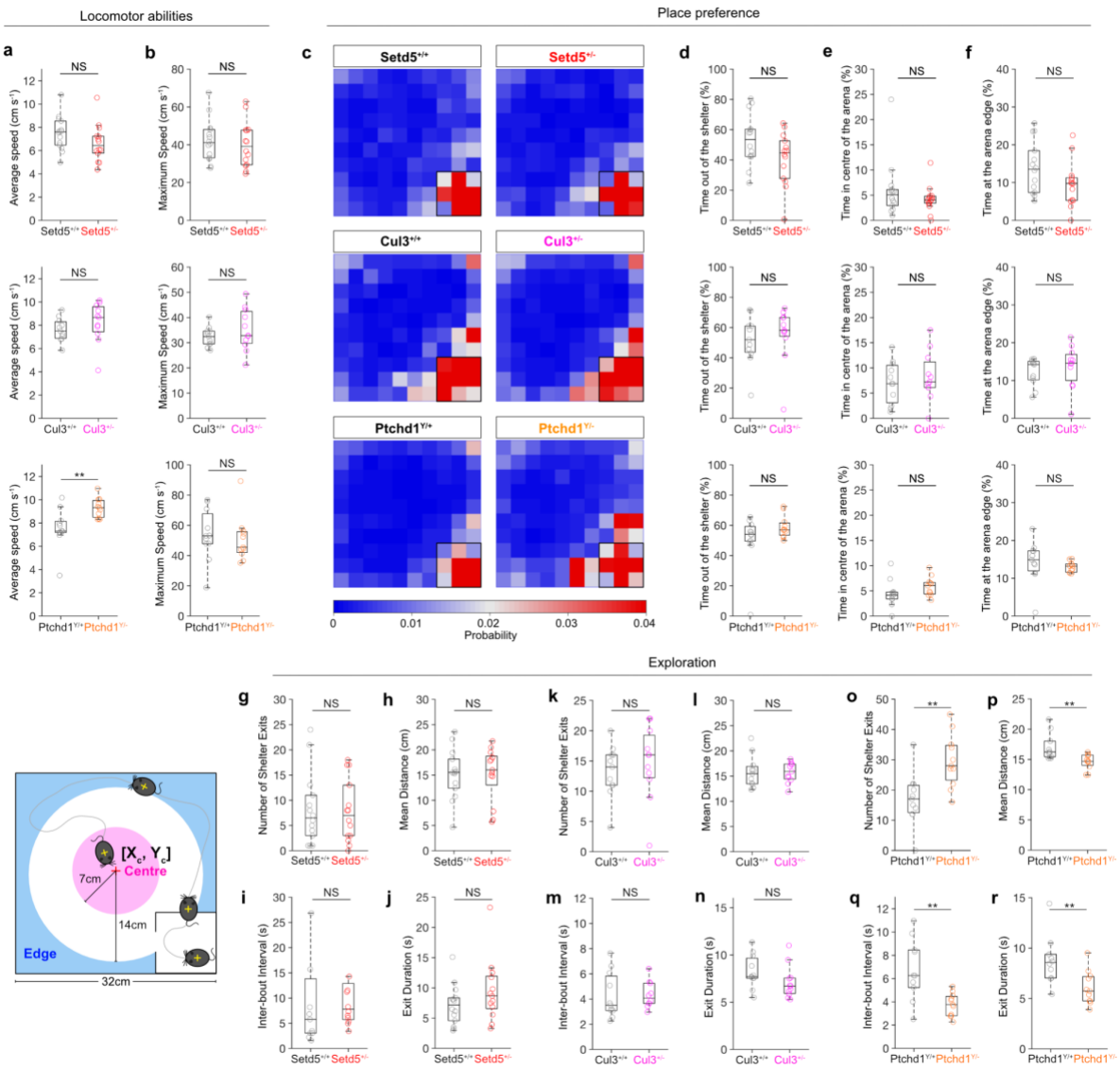

Supplementary Figure 5. *Setd5*$^{+/-}$ and *Cul3*$^{+/-}$ show typical exploratory behaviour before exposure to the looming stimulus, while *Ptchd1*$^{Y/-}$ shows a hyperactivity phenotype. a, *Setd5*$^{+/-}$ and *Cul3*$^{+/-}$ animals show similar locomotor abilities to their wild-type siblings (top, average speed: *Setd5*$^{+/+}$, 7.50 cms^{-1}; *Setd5*$^{+/-}$, 6.65 cms^{-1}, P = 0.151; middle, *Cul3*$^{+/+}$, 7.60 cms^{-1}; *Cul3*$^{+/-}$, 8.23 cms^{-1}, P = 0.3055. **b**, Maximum speed: top, *Setd5*$^{+/+}$, 42.2 cms^{-1}; *Setd5*$^{+/-}$, 40.2 cms^{-1}, P = 0.642; middle, *Cul3*$^{+/+}$, 32.5 cms^{-1}; *Cul3*$^{+/-}$, 35.2 cms^{-1}, P = 0.430). Whereas *Ptchd1*$^{Y/-}$ show an increased average speed during the pre-loom exploration (**a**, bottom, *Ptchd1*$^{Y/-}$, 9.31 cms^{-1}; *Ptchd1*$^{Y/+}$, 7.53 cms^{-1}, P = 0.003) but reached similar maximum speeds (**b**, bottom, *Ptchd1*$^{Y/+}$, 53.7 cms^{-1}; *Ptchd1*$^{Y/-}$, 50.7 cms^{-1}, P = 0.393). **c**, Place preference of all three genotypes during the open field acclimatisation. **d**, Time spent out of the shelter (top, *Setd5*$^{+/+}$, 53.5 %; *Setd5*$^{+/-}$, 40.9 %, P = 0.062; middle, *Cul3*$^{+/+}$, 51.7 %; *Cul3*$^{+/-}$, 55.6 %, P = 0.4307; bottom, *Ptchd1*$^{Y/+}$, 50.5 %; *Ptchd1*$^{Y/-}$, 58.9 %, P = 0.148). **e**, Time spent in the centre of the arena (top, *Setd5*$^{+/+}$, 6.00 %; *Setd5*$^{+/-}$, 4.20 %, P = 0.448; middle, *Cul3*$^{+/+}$, 7.10 %; *Cul3*$^{+/-}$, 8.32 %, P = 0.5323; bottom, *Ptchd1*$^{Y/+}$, 4.46 %; *Ptchd1*$^{Y/-}$, 5.86 %, P = 0.170). **f**, Time spent at the edge of the arena (top, *Setd5*$^{+/+}$, 13.9 %; *Setd5*$^{+/-}$, 9.47 %, P = 0.076; middle, *Cul3*$^{+/+}$, 12.2 %; *Cul3*$^{+/-}$, 13. 6 %, P = 0.480; bottom, *Ptchd1*$^{Y/+}$, 14.3 %; *Ptchd1*$^{Y/-}$, 13.0 %, P = 0.148). **g-r**, Exploratory behaviour during acclimatisation in *Setd5*, *Cul3* and *Ptchd1* mice. Schematic shows how the position of the mouse (yellow cross) is classified as in the centre, or at the edge of the arena given the radial distance of this point from the centre of the arena, [X_c, Y_c] (see Methods). No significant difference in behaviour in *Setd5*$^{+/-}$ animals: number of shelter exits (**g**, *Setd5*$^{+/+}$,

8.14; *Setd5*$^{+/-}$, 7.88, P > 0.999), mean distance travelled during exit (**h**, *Setd5*$^{+/+}$, 15.2 cm; *Setd5*$^{+/-}$, 15.1 cm, P = 0.981), average inter-bout interval (**i**, *Setd5*$^{+/+}$, 10.1 s; *Setd5*$^{+/-}$, 13.5 s, P = 0.230) and average exit duration (**j**, *Setd5*$^{+/+}$, 7.18 s; *Setd5*$^{+/-}$, 9.50 s, P = 0.198). No significant difference in behaviour in *Cul3*$^{+/-}$ animals: number of shelter exits (**k**, *Cul3*$^{+/+}$, 13.3, *Cul3*$^{+/-}$, 14.7, P = 0.526), mean distance travelled during exit (**l**, *Cul3*$^{+/+}$, 15.8 cm, *Cul3*$^{+/-}$, 15.7 cm, P = 0.9448), average inter-bout interval (**m**, *Cul3*$^{+/+}$, 4.26 s, *Cul3*$^{+/-}$, 4.33 s, P = 0.5035) and average exit duration (**n**, *Cul3*$^{+/+}$, 8.23 s, *Cul3*$^{+/-}$, 7.12 s, P = 0.066). *Ptchd1*$^{Y/-}$ mice were hyperactive in their exploration of the arena compared to their wild-type siblings (**o**, number of exits: *Ptchd1*$^{Y/+}$, 17.0, *Ptchd1*$^{Y/-}$, 29.5, P = 0.003; distance travelled during exit: **p**, *Ptchd1*$^{Y/+}$, 17.1 cm, *Ptchd1*$^{Y/-}$, 14.6 cm, P = 0.004; interbout interval: **q**, *Ptchd1*$^{Y/+}$, 6.76 s, *Ptchd1*$^{Y/-}$, 3.75 s, P = 0.007; exit duration: **r**, *Ptchd1*$^{Y/+}$, 8.78 s, *Ptchd1*$^{Y/-}$, 6.05 s, P = 0.007). For detailed statistics, see supplementary Table 1. *Setd5*$^{+/+}$, n = 14; *Setd5*$^{+/-}$, n = 14; *Cul3*$^{+/+}$, n = 11; *Cul3*$^{+/-}$, n =11; *Ptchd1*$^{Y/+}$, n = 11; *Ptchd1*$^{Y/-}$, n = 11 for all. Box-and-whisker plots show median, IQR and range. Shaded areas show s.e.m.. P-values: Wilcoxon's test, p-values: two-sample KS test, unless otherwise stated. For detailed statistics, see Supplementary Table 1.

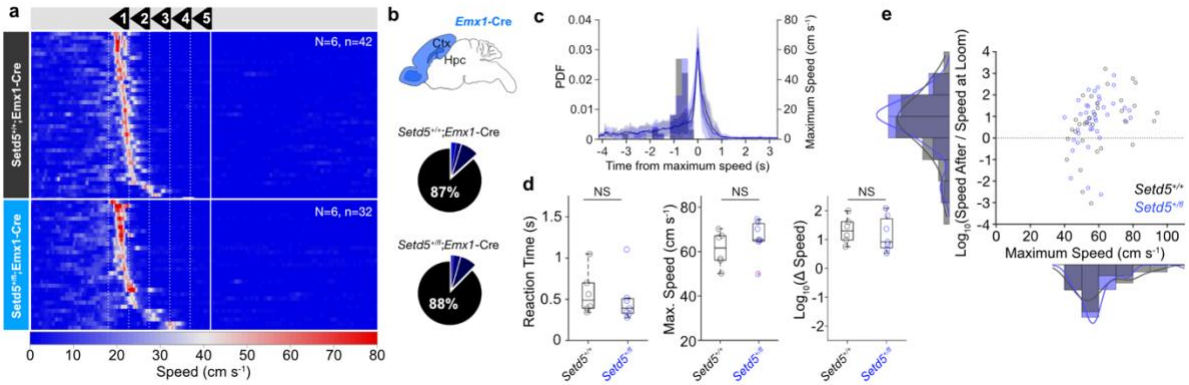

Supplementary Figure 6. Targeted haploinsufficiency of *Setd5* in the cortex and hippocampus. a, Raster plot of mouse speed in response to the looming stimuli (white, dotted vertical lines denote the start of each loom; white solid line denotes the end of the stimulus) for *Setd5*$^{+/+}$; *Emx1*-Cre (top, n = 6, 42 trials) and *Setd5*$^{+/fl}$; *Emx1*-Cre (bottom, n = 6, 32 trials), sorted by reaction time. **b**, Pictorial representation of the expression of *Emx1* in a sagittal section of a mouse brain, showing the localisation of the expression to the cortex and hippocampus (top). Proportion of trials in which the mice respond *within each loom* for *Setd5*$^{+/+}$; *Emx1*-Cre (middle) and *Setd5*$^{+/fl}$; *Emx1*-Cre mice (bottom). There is no significant difference in the proportion of trials in which the mice respond within the 1st loom (*Setd5*$^{+/+}$; *Emx1*-Cre, 0.866; *Setd5*$^{+/fl}$; *Emx1*-Cre, 0.8764, P = 0.759). Distribution of number of looms to escape, *Setd5*$^{+/+}$; *Emx1*-Cre, 28 trials, *Setd5*$^{+/fl}$; *Emx1*-Cre, 48 trials, P = 0.960, two-sample Kolmogorov-Smirnov (KS) test. **c**, Mean speed response profile of all trials where mice escape to the shelter for *Setd5*$^{+/+}$; *Emx1*-Cre (black) and *Setd5*$^{+/fl}$; *Emx1*-Cre (blue) showing similar escape kinetics, with a histogram of the distribution of the start of the loom stimulus aligned to the peak of the escape response (*Setd5*$^{+/+}$; *Emx1*-Cre, -0.633 s; *Setd5*$^{+/fl}$; *Emx1*-Cre, -0.700 s, P = 0.939). **d**, No significant difference in reaction time (Setd5$^{+/+}$; Emx1-Cre, 0.591 s; *Setd5*$^{+/fl}$; *Emx1*-Cre, 0.506 s, P = 0.468), escape vigour (*Setd5*$^{+/+}$; Emx1-Cre, 61.1 cms^{-1}; *Setd5*$^{+/fl}$; *Emx1*-Cre, 66.4 cms^{-1}, P = 0.295) or Log_{10}(Delta speed) (*Setd5*$^{+/+}$; Emx1-Cre, 0.929; *Setd5*$^{+/fl}$;*Emx1*-Cre, 0.990, P > 0.99). **e**, Relationship between Log_{10}(Delta speed) and the maximum speed reached during the escape. (Log_{10}(Delta Speed): *Setd5*$^{+/+}$; *Emx1*-Cre, 42 trials, 0.829; *Setd5*$^{+/fl}$; *Emx1*-Cre, 32 trials, 0.677, P = 0.598, two-sample KS test. Maximum escape speed: *Setd5*$^{+/+}$; *Emx1*-Cre, 42 trials, 58.8 cm s^{-1}, *Setd5*$^{+/fl}$; *Emx1*-Cre, 32 trials, 61.0 cm s^{-1}, P = 0.675, two-sample KS test).

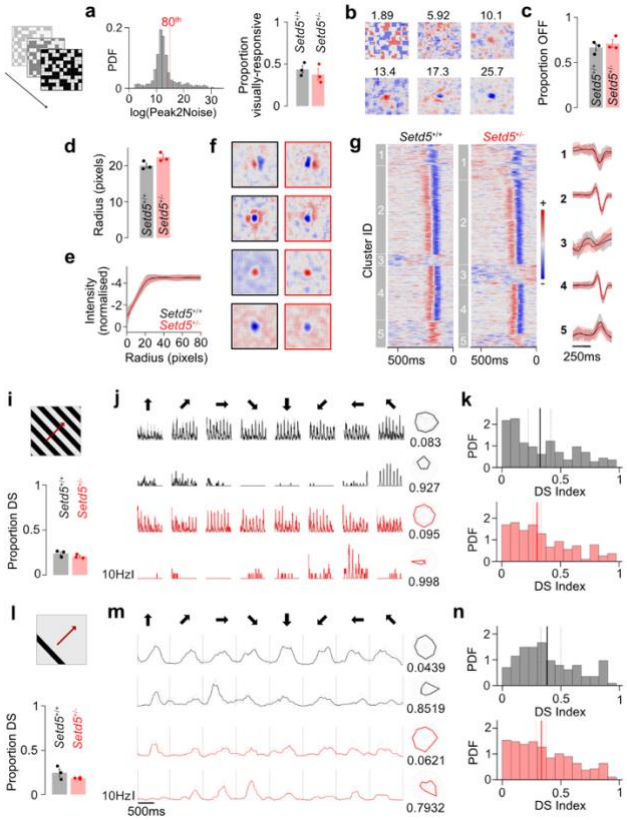

Supplementary Figure 7 - Further analysis from silicon probe data. a, Left, Distribution of log(PeaktoNoise) values of all cells. Red line indicates the 80th percentile. Right, proportion of visually responsive neurons in the sSC (*Setd5*$^{+/+}$, 0.4359, *Setd5*$^{+/-}$, 0.3666, P = 0.4000). **b**, Example spatial receptive fields at different log(PeaktoNoise) values. **c**, Proportion of visually-responsive neurons in the superficial SC (sSC) that are OFF-centres (*Setd5*$^{+/+}$, 0.679, *Setd5*$^{+/-}$, 0.738, P = 0.700). **d**, Radius of OFF-centre cells in sSC (*Setd5*$^{+/+}$, 20.2 pixels, *Setd5*$^{+/-}$, 22.4 pixels, P = 0.100). **e**, Mean ± s.e.m. of radial profile of visually-responsive OFF-centre cells (*Setd5*$^{+/+}$, 108 units, 20.4 pixels; *Setd5*$^{+/-}$, 71 units, 22.2 pixels, P = 0.307). **f**, Representative spatial receptive fields of *Setd5*$^{+/+}$ (left) and *Setd5*$^{+/-}$ (right). **g**, Left, Temporal receptive fields of visually-responsive cells in *Setd5*$^{+/+}$ (left, n = 157) and *Setd5*$^{+/-}$ (right, n = 106) grouped by cluster membership, as determined by k means (Distribution of clusters, P = 0.9545, two-sample Kolmogorov-Smirnov test). Right, mean (+/- s.e.m.) of the temporal RFs in each cluster. **i**, Proportion of direction-selective SC cells (see Methods) to full field gratings (*Setd5*$^{+/+}$, 87 of 153 units, 0.287; *Setd5*$^{+/-}$, 159 of 259 units, 0.2432, P = 0.322, Wilcoxon's test). **j**, Firing rate of example units in response to full field gratings moving in 8 different directions for *Setd5*$^{+/+}$ (black) and *Setd5*$^{+/+}$ (red) with a summary polar plot of their direction selectivity (right) and the corresponding DSI value. Bold lines show the mean response across 3 repetitions (light grey lines). **k**, Distribution of direction selectivity index (DSI) across SC units (top, *Setd5*$^{+/+}$, 153 units, median DSI = 0.323; bottom, *Setd5*$^{+/-}$, 259 units, median DSI = 0.3018, P = 0.7054, two-sample Kolmogorov-Smirnov test). Bold vertical lines represent the median DSI of all cells and dotted lines represent the median DSI of each animal. **l-n**, As for **i-k** but for single moving bar stimulus. Proportion of direction-selective SC cells (see Methods) to a moving bar stimulus (*Setd5*$^{+/+}$, 45 of 153 units, 0.243; *Setd5*$^{+/-}$, 57 of 259 units, 0.183, P = 0.143, Wilcoxon's test). **m**, as for **j** but for the moving bar stimulus. **k**, Distribution of direction selectivity index (DSI) across SC units (top, *Setd5*$^{+/+}$, 153 units, median DSI = 0.478; Bottom, *Setd5*$^{+/-}$, 259 units, median DSI = 0.417, P = 0.244, two-sample Kolmogorov-Smirnov test). Bold vertical lines represent the median DSI of all cells and dotted lines represent the median DSI of each animal.

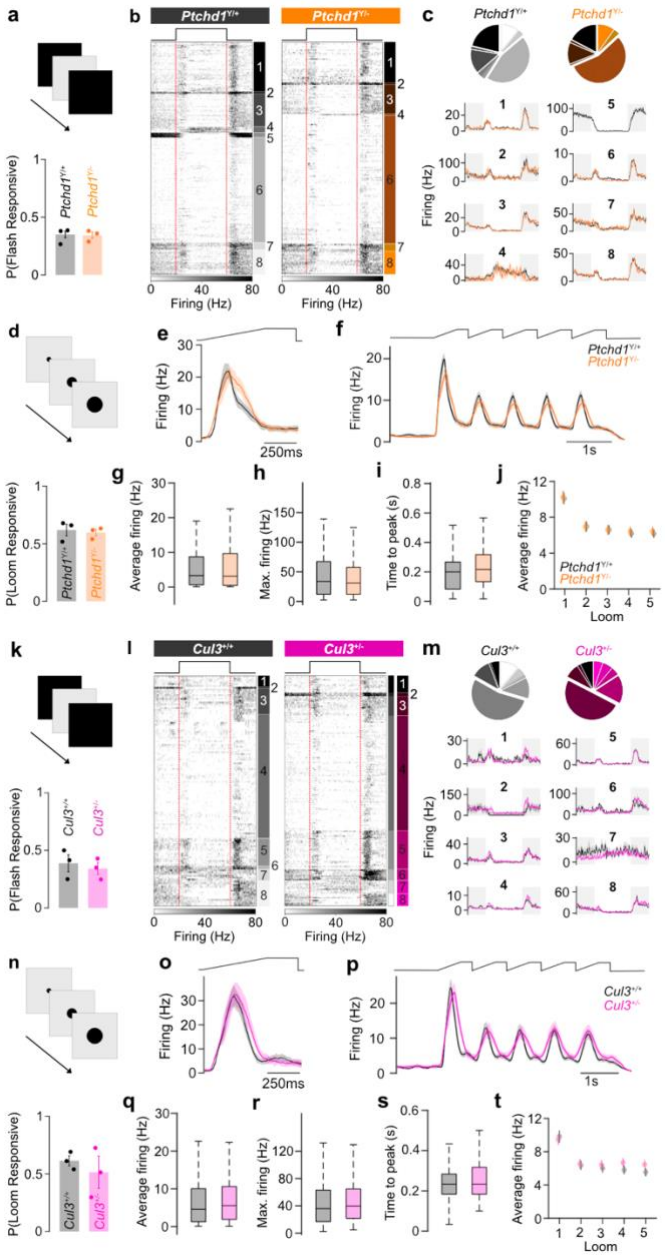

Supplementary Figure 8 - Intact visual processing in the sSC - *Ptchd1* and *Cul3*. **a**, Proportion of sSC cells that are flash responsive (*Ptchd1*$^{Y/+}$: 0.350; *Ptchd1*$^{Y/-}$: 0.343, P = 0.857, two-way *t*-test). **b**, Sorted raster plot of neural responses to a single flash stimulus. Vertical red dotted lines indicate the onset and offset of the flash stimulus. **c**, Proportion of cells in each cluster (top). Mean ± s.e.m. of the flash responses in each cluster (traces). **d**, Proportion of sSC cells that are loom responsive (*Ptchd1*$^{Y/+}$: 0.619; *Ptchd1*$^{Y/-}$: 0.597, P = 0.728, two-way *t*-test). **e**, Mean ± s.e.m. response of all of the first loom stimuli and (**f**) of the 5 consecutive loom stimuli for *Ptchd1*$^{Y/+}$ (black) and *Ptchd1*$^{Y/-}$ (orange) sSC units. **g-i**, Summary of mean, maximum and time-to-peak firing (**g**, P = 0.461; **h**, P = 0.523; **i**, P = 0.049). **n**, Average firing to a single loom across the 5-loom stimulus (p = 0.758). **k-t**, as for **a-j** but for the *Cul3* mouse model. **k**, Proportion of sSC cells that are flash responsive (*Cul3*$^{+/+}$: 0.388; *Cul3*$^{+/-}$: 0.342, P = 0.638, two-way *t*-test). **l**, Sorted raster plot of neural responses to a single flash stimulus. Vertical red dotted lines indicate the onset and offset of the flash stimulus. **m**, Proportion of cells in each cluster (top). Mean ± s.e.m. of the flash responses in each cluster (traces). **n**, Proportion of sSC cells that are loom responsive (*Cul3*$^{+/+}$: 0.614; *Cul3*$^{+/-}$: 0.514, P = 0.534, two-way *t*-test). **o**, Mean

± s.e.m. response of all of the first loom stimuli and (**p**) of the 5 consecutive loom stimuli for *Cul3*$^{+/+}$ (black) and *Cul3*$^{+/-}$ (magenta) sSC units. **q**-**s**, Summary of mean, maximum and time-to-peak firing (**q**, P = 0.214; **r**, P = 0.222; **s**, P = 0.879). **t**, Average firing to a single loom across the 5-loom stimulus (p = 0.758). P-values: Wilcoxon's test, p-values: two-way repeated measures ANOVA. *Ptchd1*$^{Y/+}$, n = 3, 263 sSC cells; *Ptchd1*$^{Y/-}$, n = 3, 202 sSC cells. *Cul3*$^{+/+}$, n = 3, 205 sSC cells; *Cul3*$^{+/-}$, n = 3, 204 sSC cells. For detailed statistics, see Supplementary Table 1.

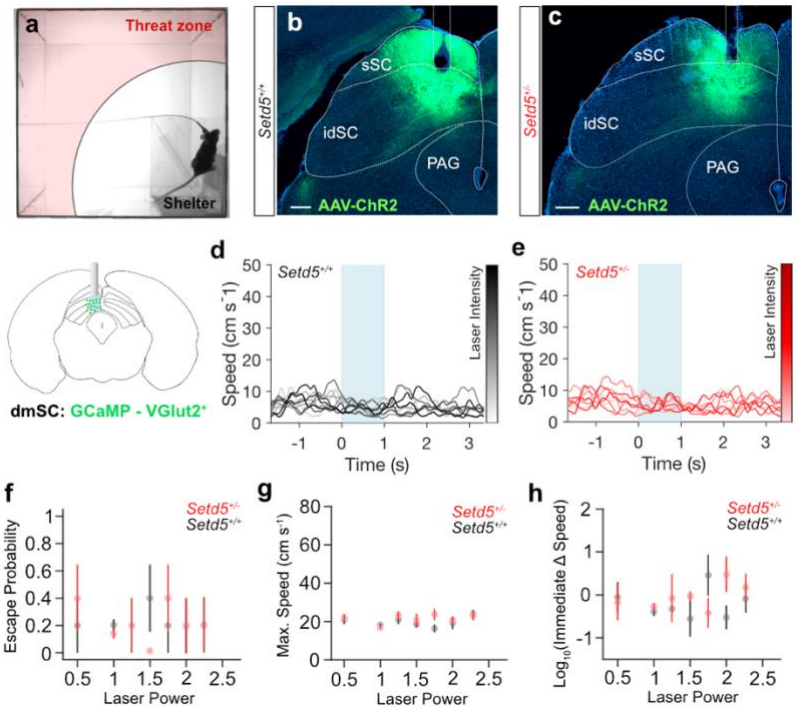

Supplementary Figure 9 - Optogenetics. a, Video frame during an optogenetics trial. **b-c**, Confocal micrographs of AAV-ChR2 expression in mSC and optic fibre location reconstruction in a *Setd5*$^{+/+}$ (**b**) and *Setd5*$^{+/-}$ (**c**) mouse. **d-e**, Mean speed responses to optogenetic stimulation at increasing laser intensities in control *Setd5*$^{+/+}$ (**d**) and *Setd5*$^{+/-}$ (**e**) mice injected with AAV-GCaMP6m. Blue shaded areas show 1 s of 10 Hz light stimulation. **f**, Relationship between escape probability and laser power (*Setd5*$^{+/+}$, r = -0.005, P = 0.955; *Setd5*$^{+/-}$, r = -0.047, P = 0.577). **g**, Relationship between maximum speed and laser power (*Setd5*$^{+/+}$, r = -0.014, P = 0.871; *Setd5*$^{+/-}$, r = 0.011, P = 0.8986). **h**, Relationship between the Log_{10}(Immediate ΔSpeed) and laser power (*Setd5*$^{+/+}$, r = -0.057, P = 0.496; *Setd5*$^{+/-}$, r = 0.283, P = 0.149). P values are Pearson's correlation. *Setd5*$^{+/+}$, n = 1, 147 trials; *Setd5*$^{+/-}$, n = 1, 145 trials. Scale bars: 200 µm.

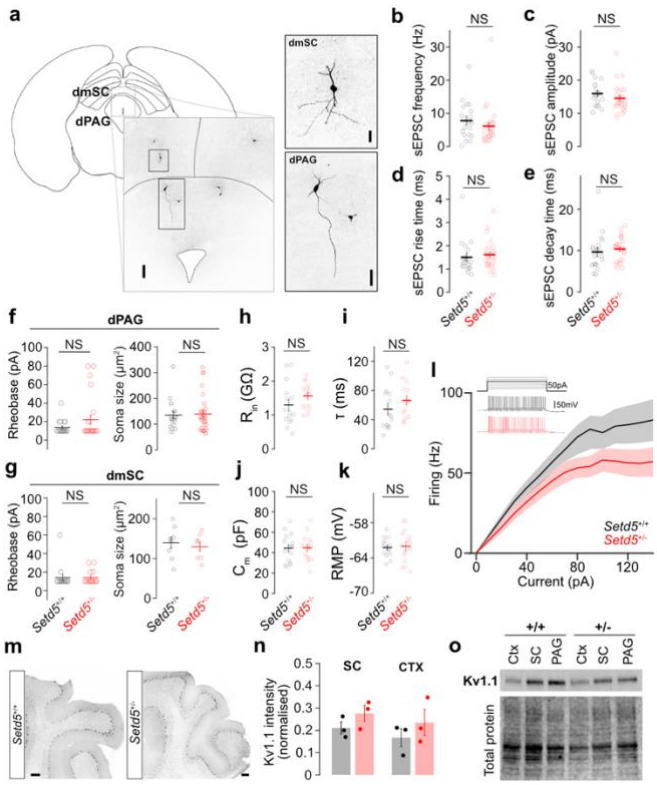

Supplementary Figure 10. Supporting *ex vivo* slice electrophysiological analysis. a, Location of dPAG (A) and dmSC (B) cells that were recorded and filled with biocytin (scale bar: 100 µm). Insets show close-ups of the biocytin-filled dPAG cells (top, scale bar: 50 µm) and dmSC cells (bottom, scale bar: 20 µm). **b-e**, Spontaneous neurotransmission in dPAG (*Setd5*$^{+/+}$: n = 6, 19 cells; *Setd5*$^{+/-}$: n = 7, 21 cells). **b**, Average sEPSC frequency (*Setd5*$^{+/+}$: 7.8 Hz; *Setd5*$^{+/-}$: 5.0Hz, P = 0.7743); **c**, average sEPSC amplitude (*Setd5*$^{+/+}$: 16.0 pA; *Setd5*$^{+/-}$: 14.0 pA, P = 0.704); **d**, average sEPSC rise time (*Setd5*$^{+/+}$: 1.50 ms; *Setd5*$^{+/-}$: 1.60 ms, P = 0.948); **e**, average sEPSC decay time (*Setd5*$^{+/+}$: 9.64 ms; *Setd5*$^{+/-}$: 10.5 ms, P = 0.838). **f**, Left, rheobase current (*Setd5*$^{+/+}$: 19 dPAG cells, 13.7pA; *Setd5*$^{+/-}$: 21 dPAG cells, 22.1 pA, P = 0.609). Right, soma size (*Setd5*$^{+/+}$: 19 dPAG cells, 135.3µm; *Setd5*$^{+/-}$: 21 dPAG cells, 139.6 µm, P = 0.899, two-tailed *t*-test.) **g**, Left, rheobase current (*Setd5*$^{+/+}$: 15 dmSC cells, 14.0pA; *Setd5*$^{+/-}$: 15 dmSC cells, 14.0pA, P > 0.999, two-tailed *t*-test). Right, soma size (*Setd5*$^{+/+}$: 9 dmSC cells, 139.9µm; *Setd5*$^{+/-}$: 9 dmSC cells, 129.6 µm, P = 0.609, two-tailed *t*-test). **h-k**, Intrinsic excitability of dmSC cells (*Setd5*$^{+/+}$: n = 4, 15 cells; *Setd5*$^{+/-}$: n = 4, 15 cells). **h**, Input resistance (*Setd5*$^{+/+}$: 1.29 GΩ; *Setd5*$^{+/-}$: 1.56 GΩ, P = 1721). **i**, Tau (*Setd5*$^{+/+}$: 54.5 ms; *Setd5*$^{+/-}$: 66.4 ms, P = 0.229). **j**, Membrane capacitance (*Setd5*$^{+/+}$: 44.4 pF; *Setd5*$^{+/-}$: 44.7 pF, P = 0.961). **k**, Resting membrane potential (*Setd5*$^{+/+}$: -62.3 mV; *Setd5*$^{+/-}$: -62.0 mV, P = 0.795). **l**, Summary of the relationship between current-injection and action potential firing in dmSC cells (*Setd5*$^{+/+}$, black, n = 15; *Setd5*$^{+/-}$, red, n = 15, P=0.066 for a main effect of genotype, two-way repeated measures ANOVA). **m**, Cerebellar Kv1.1 staining in *Setd5*$^{+/+}$ (left) and *Setd5*$^{+/-}$ (right). **n**, Western blot analysis of Kv1.1 protein content in the superior colliculus (left, *Setd5*$^{+/+}$: n = 3, 0.210; *Setd5*$^{+/-}$: n = 3, 0.275, P = 0.226, two-tailed *t*-test) and the cortex (right, *Setd5*$^{+/+}$: n = 3, 0.167; *Setd5*$^{+/-}$: n = 3, 0.235, P = 0.392, two-tailed *t*-test). *P* values are two-tailed Wilcoxon's signed-rank test, unless otherwise indicated.